Application of interferometry and cantilever-enhanced photo-acoustic spectroscopy to background-free trace gas detection

Teemu Tomberg

University of Helsinki
Faculty of Science
Department of Chemistry
A.I. Virtasen aukio 1 (P.O. Box 55)
FI-00014 University of Helsinki
Finland

Doctoral dissertation, to be presented for public discussion with the permission of the Faculty of Science of the University of Helsinki, in Auditorium D101, Department of Physics (Gustaf Hällströmin katu 2, Helsinki), on the 16th of October, 2020 at 12 o'clock.

Supervisor

Prof. Lauri Halonen
Department of Chemistry
University of Helsinki
Helsinki, Finland

Instructor

Prof. Markku Vainio
Department of Chemistry
University of Helsinki
Helsinki, Finland

Reviewers

Prof. Zhiphei Sun
Department of Electronics and Nanoengineering
Aalto University
Espoo, Finland

Prof. Jussi Toppari
Department of Physics
University of Jyväskylä
Jyväskylä, Finland

Opponent

Prof. Matti Kaivola
Department of Applied Physics
Aalto University
Espoo, Finland

ISBN 978-951-51-6562-6 (paperback)
ISBN 978-951-51-6563-3 (PDF)
http://ethesis.helsinki.fi
Unigrafia Helsinki 2020

Abstract

A trace amount of a specific gas in air, breath, or an industrial process can profoundly affect the chemistry and properties of the medium. Therefore, an accurate measurement of the concentration of the trace gas can provide invaluable information. This thesis focuses on the development of trace gas detection methods based on background-free laser absorption spectroscopic techniques. Background-free techniques possess characteristics that greatly benefit the detection of minuscule amounts of gases. These include, for example, scalability with optical power and diminished sensitivity to optical power fluctuations.

The thesis deals with two spectroscopic approaches: a novel interferometric method for broadband optical background suppression in absorption spectroscopy, and cantilever-enhanced photo-acoustic spectroscopy. We performed the spectroscopy mainly in the two atmospheric windows of 2000 to 3000 cm^{-1} and 800 to 1200 cm^{-1} found in the mid-infrared region. The employed light sources encompass various broadband and single mode laser devices, including optical parametric oscillators, optical frequency combs, and a quantum cascade laser.

The presented results include a demonstration of the interferometric background suppression with a state-of-the-art mid-infrared dual-comb spectrometer. We used the setup to compare the signal-to-noise ratio in direct absorption spectroscopy with and without the background suppression technique. The novel method was found to improve the signal-to-noise ratio by approximately a factor of five. The improvement was limited by the available optical power, and is expected to increase considerably with high power laser light sources.

In the cantilever-enhanced photo-acoustic experiments, we investigated the use of high optical power in improving the trace gas detection performance. Using a high power mid-infrared optical parametric oscillator as a laser light source, we reached a record level noise equivalent concentration of 2.5 ppt in 15 s measurement time for hydrogen fluoride. In another work, we reached a record normalised noise equivalent absorption of $1.75 \times 10^{-12}\,\mathrm{Wcm}^{-1}\mathrm{Hz}^{-1/2}$ by using an optical build-up cavity to enhance the optical power in the photo-acoustic cell. Lastly, we presented results on hyphenation of the cantilever-enhanced photo-acoustic detector and a gas chromatograph. With the hyphenation, we demonstrated the capability of quantitatively analysing a complex mixture of small to large molecular weight compounds, at a detection sensitivity far better than what can be obtained with a conventional Fourier-transform based infrared detector used in gas chromatography. Quantitative analysis of the sample would have been difficult for laser absorption spectroscopy without the chromatographic separation. The results show a great potential for laser absorption spectroscopy to be used as a detector for gas chromatography in the development of a field deployable multigas analyser.

Acknowledgements

The accomplishments in this thesis are a result of a collaboration of several bright minds. For this, I wish to thank all the people I have had the pleasure to work with in the past four years of making this thesis.

Specifically, I want to thank Prof. Lauri Halonen for accepting me in his group as a PhD student, and his complete support in all the research areas I wished to pursue.

I owe sincere thanks to Prof. Markku Vainio for being an expert instructor who has supported and encouraged me throughout my time at the University of Helsinki. Without you my time as a PhD student would have been a struggle.

I am especially thankful to Dr. Tuomas Hieta who inspired me to pursue the doctoral degree, and introduced me to photo-acoustics. Your expertise and insightful research ideas have been indispensable.

I wish to thank Prof. Konstantin Vodopyanov and his research group at the University of Central Florida for collaboration and a warm welcome to their team during my half year research visit. Furthermore, I extend my thanks to Dr. Markus Metsälä, as well as all other past and present colleagues in University of Helsinki, MIKES, Aalto, and elsewhere.

Finally, I thank my friends for the liberating moments outside the lab, and my family for their unconditional support and care. Particularly, I would like to thank Katriina for sharing the life with me, and bearing with me through this academic process.

Helsinki, October 2020

Teemu Tomberg

List of publications

This thesis is based on the following original articles, referred in the text as Article **I-IV**.

I **T. Tomberg**, M. Vainio, T. Hieta, L. Halonen, "Sub-parts-per-trillion level sensitivity in trace gas detection by cantilever-enhanced photo-acoustic spectroscopy," Scientific Reports, **8**(1), 1–7 (2018)

II **T. Tomberg**, A. Muraviev, Q. Ru, K. L. Vodopyanov, "Background-free broadband absorption spectroscopy based on interferometric suppression with a sign-inverted waveform," Optica, **6**(2), 147 – 151 (2019)

III **T. Tomberg**, T. Hieta, M. Vainio, L. Halonen, "Cavity-enhanced cantilever-enhanced photo-acoustic spectroscopy," Analyst, **144**(7), 2291 – 2296 (2019)

IV **T. Tomberg**, N. Vuorio, T. Hieta, M. Jussila, K. Hartonen, M. Vainio, T. Mikkonen, J. Toivonen, M-J. Riekkola, L. Halonen, M. Metsälä, "Broadband laser-based infrared detector for gas chromatography," Analytical Chemistry, *Submitted*, (2020)

The author has prepared the manuscripts in publications I, III and IV, and the parts of the manuscript related to the experimental work in publication II. The author has designed and built the experimental setup, performed the measurements, and analysed the measured data presented in publications I, III, IV. In publication II, the author has designed and built the experimental interferometer, performed most of the measurements and analysed the data.

Other related publications

1. **T. Tomberg**, T. Fordell, J. Jokela, M. Merimaa, T. Hieta, "Spectroscopic thermometry for long-distance surveying," Applied Optics, **56**(2), 239–246 (2017)

2. J. Karhu, **T. Tomberg**, F. Senna Vieira, G. Genoud, V. Hänninen, M. Vainio, M. Metsälä, T. Hieta, S. Bell, L. Halonen, "Broadband photoacoustic spectroscopy of $^{14}CH_4$ with a high-power mid-infrared optical frequency comb," Optics Letters, **44**(5), 1142–1145 (2019)

3. S. Larnimaa, L. Halonen, J. Karhu, **T. Tomberg**, M. Metsälä, G. Genoud, T. Hieta, S. Bell, M. Vainio, "High-resolution analysis of the ν_3 band of radiocarbon methane $^{14}CH_4$," Chemical Physics Letters, **750**, (2020)

Acronyms

Notation	Description	Page List
BF	background-free	2, 12–14, 19–21
BUF	build-up factor	32–38
CE	cavity-enhanced	36–38
CEPAS	cantilever-enhanced photo-acoustic spectroscopy	2, 4, 23–25, 30–32, 34–38, 42–47, 49
CLS	classical least squares	45
CRDS	cavity ring-down spectroscopy	1, 31
CW	continuous-wave	28, 30, 43, 49
DFB	distributed feedback laser	3, 25, 29, 33, 35
DFG	difference frequency generation	26
EC	external cavity	38, 42, 43, 49
FID	flame ionisation detector	39, 41–43, 45–47
FSR	free spectral range	32, 36, 37

Notation	Description	Page List
FTIR	Fourier-transform infrared spectrometer	16–18, 20, 40–42, 45, 48, 49
GC	gas chromatography	1, 39–45, 47, 49
ICL	interband cascade laser	2, 3
LAS	laser absorption spectroscopy	1, 3, 5, 6, 30, 40, 42, 43, 49
LO	local oscillator	18, 33
LOD	limit of detection	24, 45, 46
MIR	mid-infrared	2, 3, 21, 48, 49
MS	mass spectrometry	1, 39, 41
NEA	noise-equivalent absorbance	13, 15, 16, 21, 42, 49
NEC	noise-equivalent concentration	30, 31, 49
NIR	near-infrared	2, 48, 49
NNEA	normalised noise-equivalent absorption	24, 30, 34, 37, 49
OFC	optical frequency comb	3
OPA	optical parametric amplification	25, 26, 28
OPG	optical parametric generation	26, 28
OPO	optical parametric oscillator	2, 3, 19, 25–30, 49

Notation	Description	Page List
PA	photo-acoustic	22–25, 30, 32, 33, 35–37, 43, 44
PAS	photo-acoustic spectroscopy	1, 22–24, 30, 35–37, 42–45
PID	proportional-integral-derivative	33, 35
ppb	parts per billion, 1×10^{-9}	1, 30
PPLN	periodically poled lithium niobate	28, 29
ppm	parts per million, 1×10^{-6}	1
ppt	parts per trillion, 1×10^{-12}	2, 30, 31, 37, 49
QCL	quantum cascade laser	2, 3, 9, 25, 38, 39, 42, 43, 49
QEPAS	quartz tuning fork enhanced photo-acoustic spectroscopy	23, 24, 30
QPM	quasi phase matching	27, 28
RAM	residual amplitude modulation	9
RF	radio frequency	18
SNR	signal-to-noise ratio	13, 14, 20, 21, 45, 48
TCD	thermal conductivity detector	39, 42
TR	transmission	13, 20, 21
VUV	vacuum ultraviolet	41
WMS	wavelength modulation spectroscopy	9–11, 33

Contents

Chapter 1

Introduction

The very minor constituents of a gas mixture, typically air, are referred to as trace gases. A trace amount is commonly regarded as a volume mixing ratio from ‰ downwards, often in the part-per-million (ppm) range and less. For example, atmosphere consists mainly of nitrogen (N_2 78.1 %), oxygen (O_2 20.9 %), argon (Ar 0.934 %), and varying amounts of water vapour with the remaining consisting of trace gases. The major trace components include carbon dioxide (CO_2 400 ppm), helium (He 5.24 ppm), methane (CH_4 1.8 ppm) and nitrous oxide (N_2O 0.33 ppm), among many others. Although trace gases constitute only small portions, they can significantly impact the chemistry and properties of their environment. As an example, CO_2 and CH_4 in the atmosphere are significant contributors to global warming [1]. The presence of trace amount of ozone (O_3) in the stratosphere, protecting us from harmful UV radiation, was threatened by other trace gases CFCs in the 20th century. On the other hand, ground-level ozone is a pollutant that can trigger a variety of health problems. Many other gases, such as formaldehyde and benzene, are dangerous to health already at ppm-level requiring that they are monitored at part-per-billion (ppb) level to avoid health concerns [2–4]. In medical science, trace levels of CO_2 in humane breath are analysed for capnography and to detect gastric problems caused by *helicobacter pylori* [5].

The importance of analysis and detection of trace gas is obvious. There are numerous gas analysis techniques, which vary in selectivity and sensitivity. Some of the most highly regarded ones are gas chromatography (GC) and mass spectrometry (MS). The combination of GC and MS (GC-MS) is the base for many official standardised methods, as it currently provides the most universal platform for quantitative analysis of chemical compounds. The use of GC-MS is, however, mostly limited to offline laboratory use, whereas the applications would greatly benefit from accurate real time in situ measurements with instruments that are miniaturised and user-friendly. After the emergence of continuously tunable lasers operating near room temperature, laser absorption spectroscopy (LAS) has shown to be a technology capable of providing such instruments. The characteristic absorption spectra of molecules, also called the molecular fingerprint, makes the LAS based instruments highly selective. The development of modern sensitive LAS techniques, such as cavity ring-down spectroscopy (CRDS) [6] and photo-acoustic spectroscopy (PAS) [7], allow the detection of minute

trace amounts, down to part-per-trillion (ppt) level or below as in Article **I** and in [8, 9].

Some laser spectroscopic techniques are characterised as background-free (BF) with the general concept that if no analyte is present, the technique does not produce any signal. Examples of such techniques include Faraday rotation spectroscopy [10–12], laser-induced fluorescence spectroscopy [13, 14], and photo-acoustic spectroscopy [15, 16]. Background-free techniques are advantageous in many ways. For example, they can make use of full laser power because there is no strong background signal to saturate the detector. They are insensitive to optical power fluctuations as the signal is measured against a zero baseline. Compare to, for example, traditional transmission spectroscopy where the signal is encoded in small attenuation of the light traversed the sample. The challenge is to distinguish the wavelength dependent attenuation dips from of a large fluctuating background. The transmission measurement also needs to be normalised with a reference measurement without the analyte, which further increases the overall uncertainty. This thesis covers application of background-free spectroscopies to development of trace gas detection techniques. The emphasis is on high detection sensitivity and detection of challenging compounds. The included techniques are cantilever-enhanced photo-acoustic spectroscopy (CEPAS) in Articles **I**, **III**, and **IV**. Article **II** includes a novel interferometry-based technique for optical background suppression in absorption spectroscopy.

An important factor on the development of highly sensitive trace gas analysers is the selection of the wavelength region. The most information rich spectral region is the mid-infrared (MIR), which is loosely defined to cover the wavelengths from 2.5 to 25 µm (4000–400 cm^{-1}). In this so called molecular fingerprint region most molecules have strong fundamental rotational-vibrational transitions, making it ideal for selective and sensitive spectroscopic detection. Figure 1.1 illustrates some of the accessed MIR ro-vibrational bands, together with some of the wavelength regions used in this thesis. These regions encompass the so called atmospheric windows: 2000 to 3000 cm^{-1} and 800 to 1200 cm^{-1}, where the absorption of water vapour is small.

Laser light sources are in a crucial role in laser spectroscopy for many reasons. For example, the operation wavelength of the laser defines the accessible optical transitions, the optical power and stability has on effect on the detection limits of the instrument, and the physical size and robustness affects the usability of the instrument in applications. The MIR region has been challenging to access by laser technology. Most noteworthy are the relatively novel semiconductor lasers, such as interband cascade laser (ICL) in the 3–6 µm range [17], and quantum cascade laser (QCL) in the 6–20 µm range [18, 19], covering almost the full MIR range. These lasers are mostly used as narrowly tunable single frequency light sources. They are small in size and are therefore attractive to field applications. Another important class of laser type light sources that enables to access the MIR region is optical parametric oscillator (OPO) [20]. They are devices based on nonlinear optics which convert light from high frequency (short wavelength) to low frequency (long wavelength). The conversion is useful, since laser technology is most mature in the near-infrared region (NIR) from 0.8 – 2.5 µm (12500 – 4000 cm^{-1}). Consequently, OPOs allow NIR performance to be transferred to the MIR. Currently, the most common MIR operation range for the OPOs is 2 – 5 µm. Some nonlinear materials and NIR light sources choices allow extension of the wavelength range all the way to 10 µm or beyond [21]. However,

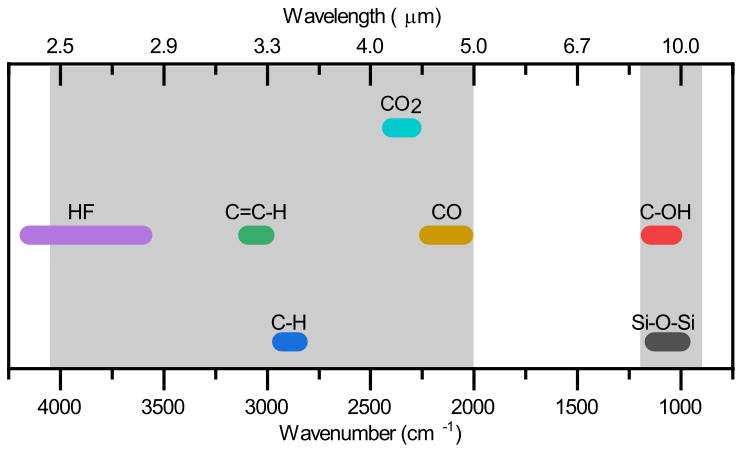

Figure 1.1: Some molecular absorption bands and wavelength regions (grey shading) accessed in this thesis.

OPOs are bulky and sensitive to mechanical disturbances, limiting their use mostly to laboratory environments.

A class of lasers that especially benefits from nonlinear frequency conversion devices, such as OPOs, is the optical frequency comb (OFC) [22]. Frequency combs are broadband laser sources whose spectra consist of thousands to millions of narrow equally spaced laser lines resembling a comb structure. They are useful as highly stable broadband light sources in applications where the high brightness and coherence of lasers are beneficial. Most LAS experiments benefit from these characteristics since, for example, the high spatial coherence of lasers allows implementation of long absorption path lengths for high detection sensitivity. An additional advantage of OFCs is exceptional wavelength stability, which is a prerequisite for highly precise spectroscopy. The stability can be exploited when the comb is used directly as a light source [23], or with a single frequency laser referenced to an optical frequency comb [24]. An ultimate example of stability is the measurement of optical transition frequencies in atomic clocks down to 1×10^{-18} level in relative uncertainty [25].

This thesis covers the use of a wide range of laser light sources and technologies, as well as the design and construction of a high power OPO in Article **I**. Near-infrared distributed feedback lasers (DFBs), ICLs, QCLs, OPOs, and are used as single frequency light sources for photoacoustic spectroscopy in Articles **I**, **III**, and **IV**. Optical frequency combs converted to the MIR with OPOs are used as coherent broadband light sources for interferometry-based background-free transmission spectroscopy in Article **II**.

The rest of the thesis is organised as follows. Chapter 2 presents an introduction to laser absorption spectroscopy from the perspective of the topic of this thesis. Chapter 3 describes the results on a novel background-free broadband absorption spectroscopy based on interferometric suppression with a sign-inverted waveform. Chapter 4 focuses on the application of a cantilever-enhanced photoacoustic spectroscopy as a highly sensitive and versatile trace gas detection method. Three approaches are presented.

The first two approaches, which are presented in Section 4.1, focus on the use of high optical power in improving the detection sensitivity to record-high levels. The third approach, discussed in Section 4.2, combines CEPAS with gas chromatography in an unprecedented way to allow an analysis of complex mixtures of large molecules, which are typically out of reach for laser spectroscopy.

Chapter 2

Laser absorption spectroscopy

This chapter provides a short introduction to the basic concepts of infrared laser absorption spectroscopy, which are appropriate to the trace gas detection techniques used in my thesis. In general terms, spectroscopy studies the interaction of electromagnetic radiation with matter. In LAS of this work the electromagnetic radiation is the infrared light of a laser, the interaction is absorption, and the matter consists of gas molecules. Gas absorbs light at wavelengths that coincide with transitions between two energy states of the molecules. These transitions are specific to each type of molecular species, providing infallible fingerprints for identification and quantification of the compounds. In the infrared, the transitions are related to change in the quantised rotational and vibrational motions of the molecules, such as stretching and bending of the molecular bonds [26]. The rotational energies are one to two orders of magnitude lower than the vibrational energies, resulting in spectral bands where a change in the vibrational energy defines the band centre and the rotational energies define the fine structure. For small molecules the infrared spectrum can be simple enough so that it is possible to probe a single transition line as shown in Figure 2.1 for CO_2. For larger molecules, the fine structure can be largely unresolved as the rotational energy levels become more densely spaced, forming continuous absorption bands.

The absorption coefficient (cm^{-1}) of a single transition can be described by the following equation [27]

$$\alpha(\nu, T, p) = N S_0(T) f(\nu, \nu_0, T, p) \tag{2.1}$$

where N is the number density of absorbing molecules (molecule cm^{-3}), $S_0(T)$ is the line intensity of a single molecule (cm^{-1}/(molecule cm^{-2})), $f(\nu, \nu_0, T, p)$ is the area-normalised line shape function ($1/\mathrm{cm}^{-1}$), and ν_0 is the centre wavenumber of the line (cm^{-1}). In a typical measurement in atmospheric conditions, N is calculated from the ideal gas law as a function of temperature T and pressure p. The line intensity $S_0(T)$ can be found from a spectroscopic database, such as HITRAN [28]. For the measurements of volume mixing ratio in trace gas detection, it maybe useful to express the number density N as a fraction of total number density of molecules: $N = c_m N_0$, where c_m is the volume mixing ratio of the absorbing molecule and N_0 is the total number density of molecules. The line intensity varies with temperature

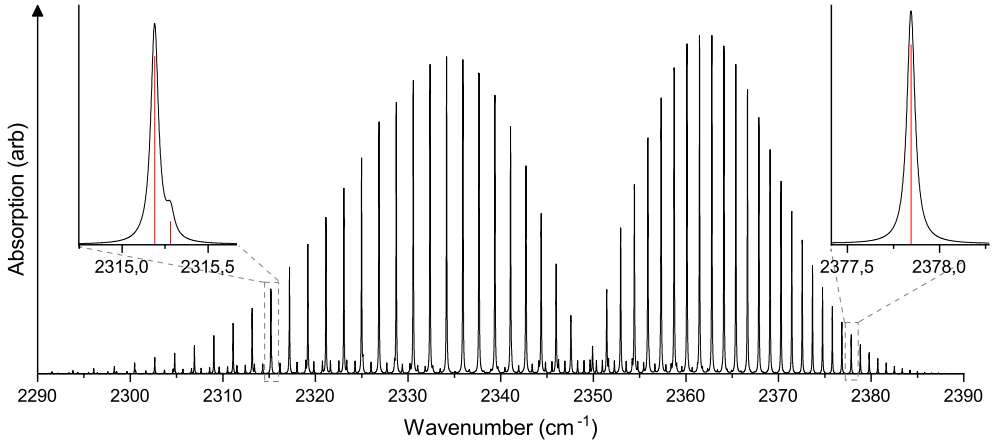

Figure 2.1: Rotational-vibrational spectrum of CO_2. The inset on the left shows two overlapping transitions while the inset on the right shows an isolated transition. The red lines indicate the line centres.

because the ground-state has a temperature dependent population. In the case of multiple transitions or gases, the total absorption is a linear sum over all contributors: $\alpha = \sum \alpha_i$.

The two most dominant underlying mechanisms determining the line shape are Doppler and collisional broadening, affected by the temperature and pressure of the gas, respectively. Thermal translational motion of the molecules gives the incident radiation a frequency shift due to the Doppler effect. The frequency shift, in the molecular frame of reference, allows the transition to be excited by a photon offset from the centre frequency, thus resulting in broadening of the line shape. The broadening follows the velocity distribution of the molecules, and can be described by a Gaussian function as

$$\begin{aligned} f_D &= \sqrt{\frac{\ln 2}{\pi}} \frac{1}{\Gamma_D} \exp\left(-(\ln 2)\left(\frac{\nu - \nu_0}{\Gamma_D}\right)^2\right), \\ \Gamma_D &= \nu_0 \sqrt{\frac{2kT \ln 2}{mc^2}} \end{aligned} \tag{2.2}$$

where Γ_D is the Doppler half-width (cm^{-1}), m is the mass of the molecule, c is the speed of light, and k is the Boltzmann constant. The Doppler half-width is in the order of 100 MHz ($0.0033\,\mathrm{cm}^{-1}$) in a typical LAS trace gas detection application of light molecules in atmospheric temperature.

The movement of the molecules also leads to intermolecular collisions that exchange energy and shorten the lifetime of the excited state. This results in pressure dependent collisional broadening and shift in the central frequency of the line. The broadening mechanism is described by a Lorentzian line shape function as

$$f_L = \frac{1}{\pi} \frac{\Gamma_L}{(\nu - \nu_0 - \Delta)^2 + \Gamma_L^2} \tag{2.3}$$

with Γ_L being the pressure-broadened line half-width and Δ being the pressure-induced line shift. The extent of the collisional effects depends on the collisional partner. Coefficients for air and self broadening are tabulated in HITRAN. Typical values for Γ_L in air are in the order of 3 GHz/atm ($0.1\,\mathrm{cm}^{-1}$/atm), and the shifts in the central frequency in the order of -30 MHz/atm ($-0.001\,\mathrm{cm}^{-1}$/atm).

At high pressures the collisional broadening dominates. As the pressure decreases the Doppler broadening becomes a greater contributor. In the simplest case, one of these two functions can be used as such in the fitting process for retrieval of experimental parameters, such as the target gas number density N. Normally, both Doppler and pressure broadening have significant contributions to the line shape, and more sophisticated models are required. A popular line shape function is the Voigt function, which is a convolution of a Gaussian and Lorentzian function. It gives a good representation of the line shape for many applications. For the most accurate measurements, the current recommendation is the more complex Hartmann-Tran profile [29]. It is sophisticated enough to capture the various contributions of molecular motion to the line shape, including the molecular speed dependent relaxation rates and the effect of collisional velocity changes to the Doppler broadening. Several other line shape functions also exist with varying accuracy and complexity. They are summarised in [29].

Absorption can be measured either by observing a change in the state of the gas, or the state of the probing light. The first of these approaches is referred to as "indirect" technique, while the latter approach as "direct". An example of measuring a change in the state of the gas is photo-acoustic spectroscopy, discussed in Chapter 4. A change in the state of the light is, in almost all cases, measured by a photodetector, which responses to the total optical power incident on the detector. As light traverses an absorbing medium, its optical power is attenuated exponentially according to the Beer-Lambert law as

$$P = P_0 e^{-\alpha L} \tag{2.4}$$

where L is the optical path length and P_0 is the incident optical power. In a usual experiment with a tunable diode laser and a photodetector, the detector records transmitted optical power P as a function of wavelength as the laser wavelength is scanned over the absorption line. The incident power may be measured in a similar way or estimated from the measurement. The result $T(\nu) = P(\nu)/P_0(\nu)$ is referred to as the transmission spectrum, and $A(\nu) = -\ln\left(P(\nu)/P_0(\nu)\right) \approx 1 - T(\nu)$ as the absorption or absorbance spectrum. In this thesis, we adopt the Napierian form of absorbance, which is better suited for trace gas spectroscopy. However, the reader should be aware that the common way in analytical sciences is to define the absorbance as a base-10 logarithm. The measurement of absorption directly or indirectly allows one to obtain the number density N, or the respective mixing ratio c_m of an analyte in the medium. Usually the analysis is performed by fitting a chosen line shape function to the measurement in order to extract the line area $A_{int} = NS_0L$. A suitable line shape function may be chosen by inspecting the residual of the fit. In case the residual shows features clearly distinguishable from noise, it may be necessary to increase the accuracy of the model. If the pressure and temperature are well known, the measurement can be sped up by recording the absorption only at the line centre $A_0 = NS_0Lf(\nu_0, \nu_0, T, p)$. In some applications, the absorption measurement is also used to determine the tem-

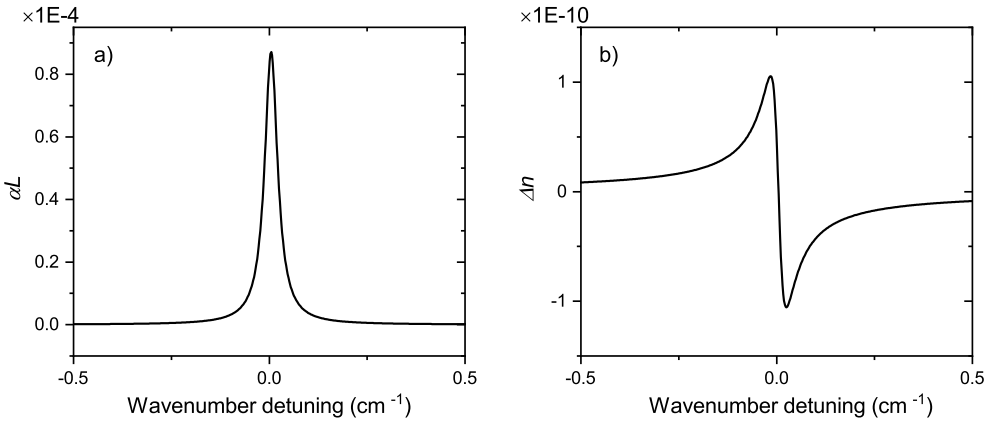

Figure 2.2: An example of a) absorption and b) refractive index change associated with a single transition.

perature or pressure of the gas as in Article **1** or in many combustion applications [30].

Some of the spectroscopic methods are sensitive to the phase of the electromagnetic wave. In such case, it is necessary to write the line shape function in a complex form to account for the dispersion associated with absorption. Equation 2.1 then becomes

$$\begin{aligned} \alpha_c(\nu, T, p) &= NS_0(T)\mathrm{Re}(f(\nu, \nu_0, T, p)) + iNS_0(T)\mathrm{Im}(f(\nu, \nu_0, T, p)) \\ &= \alpha(\nu, \nu_0, T, p) + i\beta(\nu, \nu_0, T, p) \end{aligned} \tag{2.5}$$

where the real part of f yields the absorption coefficient and the imaginary part the dispersion coefficient β. Dispersion means that the refractive index of the medium is wavelength dependent. Here, the dispersion originates from absorption according to Kramers-Kronig relations, which state that an absorptive medium must experience dispersion and vice versa [20]. The associated refractive index change may be written as $\Delta n = -\beta/(4\pi\nu)$. Figure 2.2 shows an example of α and Δn for a single absorption line.

The interaction of light with the medium is written for the electric field as

$$E = E_0 e^{-\alpha L/2} e^{-i\beta L/2} \tag{2.6}$$

which reduces to Equation 2.4 in case the optical power $P \sim |E|^2$ is detected.

Wavelength modulation spectroscopy

As outlined in the introduction, the usual transmission measurements need to distinguish the absorption signal from a large fluctuating background, which sets the limit for the smallest detectable absorption. Modulation techniques can improve the performance of a transmission measurement by translating the detection to higher frequencies with less noise and by removing the need to measure the difference between

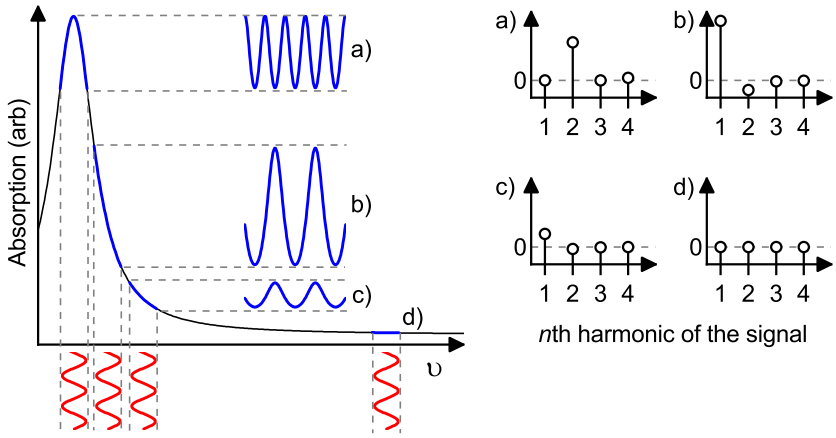

Figure 2.3: Formation of WMS absorption signal (in blue) as the centre wavenumber of the laser (in red) is scanned over an absorption line. Figures on the right show decomposition of the WMS absorption signals to their harmonic lock-in signals.

two large signals: the detector signal in the presence and absence of the analyte. One of the most popular modulation techniques is wavelength modulation spectroscopy (WMS) [31]. In WMS, the experimental arrangement remains the same as in direct transmission measurement, with the exception that the wavelength of the laser is modulated around a centre wavenumber ν_c. Usually the modulation waveform is sinusoidal, written as $\nu(t) = \nu_c + \nu_a \sin(2\pi f_m t)$, where ν_a is the amplitude of the modulation and f_m is the modulation frequency. At the detector, the signal is demodulated with a lock-in amplifier at nth harmonic (nf_m, $n = 1, 2, 3, \dots$) of the modulation frequency. The modulation frequency is smaller than the linewidth of the probed transition, usually in the kHz to MHz range, differentiating the technique from frequency modulation spectroscopy, in which the modulation frequency is in the order of the linewidth or larger. Instead, the modulation amplitude is found, often experimentally, to produce the strongest WMS signal when being comparable to the linewidth of the transition.

Figure 2.3 exemplifies the formation of a WMS signal. A photodetector is insensitive to small changes of the wavelength. Therefore, in the absence of absorption, the optical power reaching the detector is the same as that emitted by the laser, as in case d) of Figure 2.3. The demodulated lock-in signal is zero for all the harmonics since the detector signal is constant. Hence, WMS can be considered as a background-free technique although the signal level at the photodetector is still high. In practice, residual amplitude modulation (RAM) often causes a background signal. For a common semiconductor laser, such as a QCL, the wavelength modulation by the injection current creates a significant RAM component at the 1st harmonic. The reason is that the optical power of the laser varies, as a first approximation, linearly with the injection current. It is therefore more common to detect the 2nd harmonic signal, which is largely background-free also for semiconductor lasers. In addition to modulation by the injection current, interference effects in, for example, etalons may cause RAM.

In the presence of absorption, the transmitted optical power of the laser is modulated by the sample absorption, as in cases a)-c) in Figure 2.3, producing a response

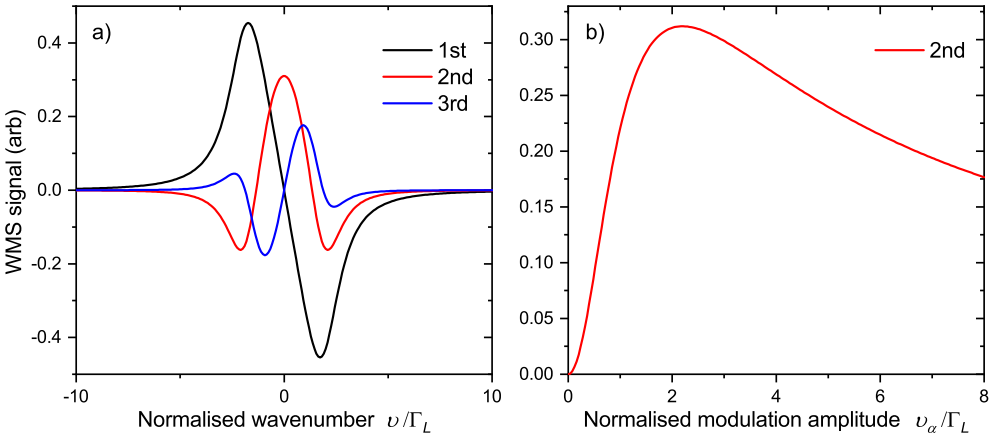

Figure 2.4: a) Illustrations of the 1st, 2nd and 3rd harmonic WMS signals for a Lorentzian line shape function. b) 2nd harmonic WMS signal at the centre (peak) of the line as a function of modulation amplitude.

on the photodetector that is directly proportional to the absorbance. In a), the laser scans over the peak of the line, producing a strongly non-linear response on the absorption signal at higher (even) harmonics. In b) and c), the response on the absorption signal is more linear, producing modulation mostly at the 1st harmonic. An accurate description of the proportions of the harmonics can be developed by substituting the wavelength modulation function to Equation 2.1 for absorption and developing the result as a Fourier series. The nth Fourier component is then proportional to the nth harmonic lock-in signal. Analytical expressions for the Fourier components of the simplest Gaussian and Lorentzian line shape functions exist [31], whereas the coefficients for more complex functions, such as the Voigt, need to be solved through different approximations or numerical approaches [32, 33]. Qualitatively, the produced lock-in signals resemble the derivatives of the absorption feature, with the nth harmonic representing the nth derivative.

Figure 2.4 a) illustrates the 1st, 2nd, and 3rd harmonic WMS signals simulated for a Lorentzian line shape as a function of normalised wavenumber: ν/Γ_L. The modulation amplitude was chosen to maximise the 2nd harmonic peak signal. For a Lorentzian line shape, the maximum peak value is found for a normalised modulation amplitude $\nu_a/\Gamma_L = 2.2$, as shown in Figure 2.4 b) [31]. Useful observations include that the odd harmonics experience a zero crossing at the line centre, where the even harmonics reach maxima. Simultaneously, higher harmonics are weaker than the lower ones. The 2nd harmonic is often found most useful for trace gas detection, while the 1st or the 3rd harmonics can be used, for example, to lock a laser wavelength to the line centre. More about the use of wavelength modulation technique for laser locking can be found in Subsection 4.1.2.

A drawback from using WMS is that the capability for absolute quantitative measurements without calibration is practically lost. A number of research articles have been published on methods described as 'calibration-free' that partly overcome this deficiency, for example, by carefully calibrating the laser tuning characteristic in order

to retrieve the absolute absorption signal from a WMS measurement [34]. However, for some spectroscopic techniques, such as photo-acoustic spectroscopy, the loss of absolute absorption signal is irrelevant as the technique in any case requires a calibration. Chapter 4 discusses photo-acoustic spectroscopy in more detail.

Chapter 3

Interferometric background suppression

In conventional transmission spectroscopy light passes through a sample and its attenuation is recorded at each wavelength. As a result, one obtains a transmittance spectrum with the emission profile of the light source as a background. The molecular information is recorded in the small absorption dips as described by Equation 2.4, which poses a challenge to the instrumentation. Fluctuation in the background spectrum P_0 determine whether the dips can be detected or not. The background stability is in most cases dominated by spectral power density fluctuations of the light source. In addition, the measurement of small deviations from a comparatively large background signal requires a high-dynamic-range detector. Background-free spectroscopic techniques can avoid these challenges and reach the intrinsic noise limit of the detector. This chapter presents the theory and experimental results of a novel background-free broadband absorption spectroscopy based on interferometric background suppression with a sign-inverted waveform.

3.1 Theory of the suppression method

A transmission measurement can be transformed to a background-free measurement by optically subtracting the background spectrum from the transmission spectrum. As a result, the measurement will show emission-like peaks on a zero background instead of absorption dips. Optical subtraction of two spectra is possible by interference of their optical fields at opposite phases. Lasers offer high enough spatial coherence so that a high level of subtraction is possible. This section presents a quantitative description of the process and interpretation of the produced signal. We begin by following the approximations laid in Article **II**, followed by a more rigorous description of a realistic experiment in the formalism of the common two-beam interference equation.

A simple approximation of the optically subtracted background-free measurement can be derived by first writing the background spectrum in electric field form as $E_B(\nu) = E_0(\nu)$, and the transmission spectrum as $E_T(\nu) = -E_0(\nu)e^{-A(\nu)/2}$. The minus-sign in front of E_0 designates opposite phase (π phase difference), and the term

$e^{-A(\nu)/2}$ describes attenuation by molecular absorption according to Beer's law with $A(\nu)$ being the wavenumber dependent Napierian absorbance. In a normal transmission measurement one would record $E_T(\nu)$ with a spectrometer equipped with a photodetector, producing a spectrum written as $P_{tr} \sim E_0^2 e^{-A(\nu)}$. For the usual case of $A(\nu) \ll 1$, this can be approximated as

$$P_{tr} \sim P_0(1 - A(\nu)), \tag{3.1}$$

where the absorption signal is found as the background $P_0 = E_0^2$ minus the transmission measurement: $P_0 - P_{tr} = P_0 - P_0(1 - A(\nu)) = P_0 A(\nu)$. The signal-to-noise ratio for a single absorption line is

$$\mathrm{SNR}_{tr} = \frac{A_0}{\sigma_{las}}, \tag{3.2}$$

where σ_{las} is the relative standard deviation of the optical power spectral density of the laser, and A_0 is the peak absorbance of the spectral line. Here, we have assumed a typical case where the laser noise dominates over other noise sources.

In the case of optical background suppression, the two beams E_B and E_T interfere and the measured signal $P_{bf}(\nu)$ is proportional to $P_{bf}(\nu) \sim |E_B + E_T|^2 = |E_0 - E_0 e^{-A(\nu)/2}|^2$. For $A(\nu) \ll 1$, this can be approximated as

$$P_{bf} \sim \frac{P_0}{4} A^2(\nu), \tag{3.3}$$

describing a background-free absorption signal. The signal-to-noise ratio is

$$\mathrm{SNR}_{bf} = \frac{P_0}{4} \frac{A_0^2}{\sigma_{det}}, \tag{3.4}$$

where σ_{det} is the noise equivalent power of the photodetector.

In most cases the absorbance is small, from which it follows that $A_0^2 < A_0$ and that the magnitudes of P_0, σ_{las}, and σ_{det} determine whether it is the P_{bf} or P_{tr} approach that gives a higher SNR. For narrow spectral lines with a small integrated total absorbance over the spectral range of interest, $P_{bf} \ll P_{tr}$, and it is possible to increase the optical power significantly in the BF case compared to the transmission (TR) case without detector saturation. Therefore, with these assumptions, the BF approach can give much higher SNR with the available laser power being most likely the limiting factor. As a case study, let us calculate the optical power required for a typical absorbance measurement with noise-equivalent absorbance (NEA) of 0.1%. By setting $\mathrm{SNR}_{bf} = \mathrm{SNR}_{tr}$, we find that $P_0 = \frac{\sigma_{det}}{\sigma_{las}} \frac{4}{A_0}$. By choosing $10\sigma_{las} = \sigma_{det}$ and assuming that the laser noise dominates in the transmission measurement, we can substitute $A_0 = 10^{-3}$ and obtain $P_0 = 400$. The BF measurement requires over 400 times higher optical power than the TR measurement in order to reach better NEA. Such power levels are found possible when comparing the optical power of available lasers and a typical saturation limits of detectors. However, it should be noted that even though the NEA would not improve, the quadratic nature of the BF method means that the SNR for $A_0 >$ NEA is still higher than in the transmission measurement. A high SNR is important for accurate measurements.

We have neglected several non-idealities in the above treatment. To derive a more accurate representation, we use the two beam interference equation [20] and include

a factor $\rho(\nu)$ to describe the difference in the intensities of the two interfering optical beams, and a variable $\phi(\nu)$ as the deviation from π phase difference. The reader should be aware that the imbalance factors ρ and ϕ are defined differently from Article **II** in order to comply with the formalism of the two-beam interference. Also, the absorbance is now written in complex form as $A(\nu) = a(\nu) + ib(\nu)$. Hence, $E_B(\nu) = E_0(\nu)$, and $E_T(\nu) = -\sqrt{(1-\rho)E_0(\nu)e^{-a(\nu)-i(b(\nu)+\phi(\nu))}}$. The two beam interference equation,

$$P = P_1 + P_2 + 2\sqrt{P_1 P_2}\cos\theta, \tag{3.5}$$

is then written as

$$P_{bf} \sim P_0\left(1 + e^{-a}(1-\rho) - 2\sqrt{e^{-a}(1-\rho)}\cos\left(\frac{b+\phi}{2}\right)\right), \tag{3.6}$$

which approaches P_0 for very large absorption ($a \to \infty$), indicating the saturation level of the method. From Equation 3.6 it follows that if P_0 is measured, the proposed background-free spectroscopic method provides quantitative spectral information the same way as a traditional transmission measurement, with the exception that the BF-signal is nonlinear of nature. In other words, the information from spectral databases, such as HITRAN, can be used to extract, for example, the sample gas volume mixing ratio from a BF measurement.

To better understand Equation 3.6, we may approximate it for $a, \phi, \rho \ll 1$ by substituting $\cos(\theta) \approx 1 - \theta^2/2$, $e^{-a} \approx 1 - a + a^2/2$, $\sqrt{e^{-a}} \approx 1 - a/2 + a^2/8$, and $\sqrt{1-\rho} \approx 1 - \rho/2 - \rho^2/8$. Then, by neglecting all third and higher order terms, we end up with

$$P_{bf} \approx \frac{P_0}{4}\left(\phi^2 + \rho^2 + b^2 + 2a\rho + 2b\phi + a^2\right), \tag{3.7}$$

where we the term b is may be omitted for simplicity. The inclusion of b is discussed later in this section. The approximation shows that a mismatch in either amplitude or phase balance of the optical fields will result in a background signal.

The signal-to-noise ratio should now include the optical power related noise terms. These are the term associated with the laser technical noise $P_{N,las} = \sigma_{las}P_0/4(4\phi^2 + \rho^2)$, the quantum (shot) noise of the laser power at the detector $P_{N,sht} = (P_0/4(\phi^2 + \rho^2)hc\nu\Delta f)^{1/2}$, and the detector noise term $P_{N,det}$. Here, $hc\nu$ is the photon energy with ν expressed in wavenumber units, and Δf is the detection bandwidth. Unit quantum efficiency is assumed. We write the SNR as

$$SNR_{bf} = \frac{\frac{P_0}{4}(2\rho a_0 + a_0^2)}{\sqrt{(P_{N,las})^2 + (P_{N,sht})^2 + (P_{N,det})^2}}. \tag{3.8}$$

Again, if the detector noise dominates, $SNR_{bf} = (P_0/P_{N,det})(\rho a_0/2)$ for $a_0 \ll \rho$ and therefore, the SNR improves with increasing optical power similarly to Eq. 3.4. At some point, the shot noise and then the laser noise will start to dominate. If the laser noise dominates over other noises, the SNR equation simplifies to $SNR_{bf} = (2\rho a_0 + a_0^2)/(\sigma_{las}(4\phi^2 + \rho^2))$. Now, increasing the laser power does not improve the SNR. Instead, one needs to decrease ρ and ϕ.

Assuming unlimited optical power, the background-free absorption spectroscopy will eventually reach the laser noise limited operation regime. This limit determines the

lowest detectable absorbance. In Figure 3.1, the lowest detectable absorbance, or the noise-equivalent absorbance, is plotted as a function of the imbalance coefficients ρ and ϕ, with a laser noise value of σ_{las} =1 $\times$ 10^{-3}. In a normal transmission measurement, the noise-equivalent-absorbance is equal to the value σ_{las} for the laser noise. This limit is highlighted with a thick contour line in the figure. As can be seen, even in a modest case of ρ = 0.1, the NEA will improve from the normal transmission measurement (NEA=1 $\times$ 10^{-3}), as long as the phase ϕ is controlled to a sufficient accuracy. The same applies for a shot noise limit.

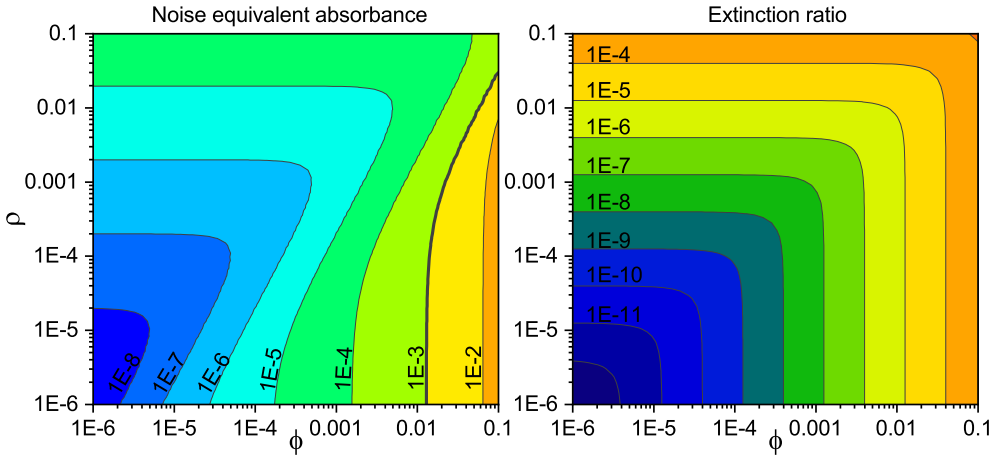

Figure 3.1: Calculated noise-equivalent absorbance and the corresponding extinction ratio for σ_{las} =1 $\times$ 10^{-3} in the case of no absorption related phase change b.

The graph is divided diagonally into two regimes: the intensity mismatch (ρ) dominated regime on the top-left side and the phase imbalance (ϕ) dominated regime on the bottom-right side. On the ρ side, the absorption features are symmetric as in a normal transmission measurement. On the ϕ side, however, the absorption related signal is weak compared to the noise. The lines become asymmetric as the absorption related phase change b, illustrated in Figure 2.2 b), dominates the molecular signal. The phase related signal was excluded from the analysis in Figure 3.1 for simplicity. The inclusion of b to the analysis would improve the performance in the ϕ limited regime. When the interferometer is offset from the destructive interference (equal to large ϕ), the signal at the detector becomes highly sensitive to small phase changes, which is in this case are caused by absorption. Even though the direct absorption related signal was buried in noise, the phase related signal may be observed. The detection scheme is in this case similar to the operation of the interferometer based advanced gravitational wave detectors [35].

To evaluate the performance of a background suppression interferometer, we define the extinction ratio Δ_P as the ratio of the suppressed optical power (destructive interference) to the initial optical power (constructive interference). The initial power is $4P_0$ and the suppressed optical power may be approximated as $P_0/4(\phi^2 + \rho^2)$ so that the extinction ratio is written as

$$\Delta_P = \frac{1}{16}\left(\phi^2 + \rho^2\right). \tag{3.9}$$

The extinction ratio is plotted together with the NEA in Figure 3.1.

3.2 Practical implementation

A practical implementation of the presented background-free absorption spectroscopy is based on a two-beam interferometer. In a two-beam interferometer a beam of radiation is divided into two by a beamsplitter, and recombined after passing through separate optical paths. For the purpose of optical background suppression, one of the beams should pass through the sample under investigation while the other beam through a reference. The reference can be, for example, vacuum, air, or another sample. The beams should be combined after a π phase shift difference introduced to one of the beams. For monochromatic light, the phase change can be achieved by simply changing the optical path length by one half wavelength: $\lambda/2$. The acquired propagation phase change $\Delta\phi$ is given by

$$\Delta\phi = 2\pi\frac{\Delta l}{\lambda} \tag{3.10}$$

where Δl is the difference in the optical path length. The propagation phase change is wavelength dependent and therefore not suitable for broadband background suppression. Achromatic phase shift of π is possible by several methods, including the use of a Gouy phase shift by light propagating through a focus [36], a pair of mirror-symmetric periscopes to flip the beam geometrically [37], or a pair of right-angle Fresnel rhombs used as a pair of quarter-wave plates [38]. In our work, we study another elegant solution exploiting the phase change of π between reflection of an internal versus external surface of a dielectric medium [20].

Figure 3.2 presents a possible realisation of an optical background suppression interferometer according to the outlined principle. The solution is based on a common Michelson-type interferometer, which is the base of a Fourier-transform infrared spectrometer (FTIR) [39], a standard analytical tool in infrared spectroscopy. For the context of this work, it is useful to briefly overview the operation principles of an FTIR. A spectrometer refers to a scientific instrument that can resolve the spectral components of a light source. In an FTIR, the resolving power is based on the interference signal produced at the output of a Michelson interferometer on a photodetector as the optical path difference between the arms of the interferometer is scanned by translating one of the retroreflecting mirrors. The optical path difference introduces a chromatic phase shift according to Equation 3.10. Substituting the equation for the phase shift to Equation 3.5 for two beam interference, we find that the output of the interferometer at wavelength λ consists of a sinusoidally oscillating signal as a function of the path difference Δl. This output signal is referred to as the interferogram. For a polychromatic light source, the interferogram is the superposition of all the monochromatic interferograms. The interferogram of a broadband source consists of a sharp peak at the zero optical path difference, followed by oscillating tails at larger Δl, which contain the detailed spectral information. In fact, the spectral resolution of an FTIR in reciprocal centimetres is proportional to the maximum optical path

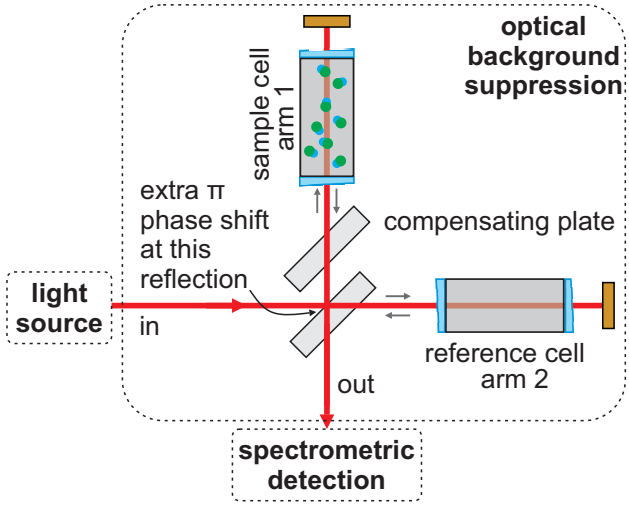

Figure 3.2: A schematic illustration of a dual-beam interferometer-based realisation of the optical background suppression technique.

difference Δl_{max}. The optical spectrum is obtained by taking the Fourier transform of the interferogram.

For the use of a Michelson interferometer in optical background suppression spectroscopy, the optical path difference should be zero. The sample is introduced in one of the identical sample cells, which are placed in both arms of the interferometer. The beamsplitter of the interferometer is a thick dielectric slab and the reflection takes place on one of the surfaces. The purpose of the other plate, with identical material and thickness, is to compensate for the longer path the other beam travels through the beamsplitter. The requirements for the symmetry of the optical paths are stringent. Group delay and group delay dispersion need to be compensated, which requires strictly equally thick transmissive optical components. Also, the shape of the optical wavefronts needs to be preserved, which requires highly flat optical surfaces.

The idea of optical background suppression has seen various realisations along the years. Perhaps the earliest work on the topic relates to the dual-beam experiments with FTIRs. The dual-beam experiments sought to suppress the background related optical interference signal on the detector, together with source intensity noise, by superimposing the two opposing phase outputs of an interferometer on the same detector [40–42]. A main complication in the early dual-beam experiments with incoherent light sources was the optical construction of the interferometer so that it would provide access to the second output with the opposing phase. In normal arrangement, as in Figure 3.2, the second output beam returns to the source. Furthermore, none of the work on incoherent light sources addressed the problem of detector saturation because of a high optical DC-signal level and the related requirement for a high dynamic range. In a more recent work with single frequency lasers, the DC level at the detector was nullified by adjusting the phase with propagation delay [43, 44]. In reference [45] the authors describe the same principle for a broadband light source, although the adjustment of propagation delay cannot provide an achromatic π phase shift. In reference

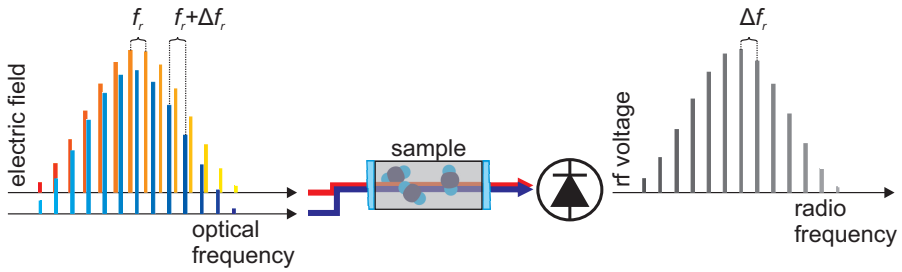

Figure 3.3: The principle of symmetric dual-comb spectroscopy presented in the frequency domain.

[46], the authors came to a similar realisation to the one presented in this theses with a broadband laser source and achromatic phase retardation.

The optical background suppression technique is a spectral manipulation method, which is independent of the detection method. The technique is applicable to broadband spectroscopic detection methods such as FTIR and grating spectrometers, or simple broadly tunable single frequency lasers, such as external cavity diode lasers. An especially advantageous detection method for the optical background suppression is the recently developed Fourier-transform based dual-comb spectroscopy [47]. Dual-comb spectroscopy is a multi-heterodyne detection method, which makes use of the special comb like spectral structure of the frequency combs. In optical heterodyne detection, a signal beam at the optical frequency ν_1 is coherently combined on a photodetector with a local oscillator (LO) beam that has a slightly different optical frequency ν_2. Interference of the signal and LO beams produces a beat signal on the photodetector at the difference frequency $|\nu_2 - \nu_1|$. Dual-comb spectroscopy is called a multi-heterodyne method because the spectrum of a frequency comb consists of thousands to millions of individual equidistant laser lines. When two of such frequency combs are coherently combined, each individual line pair produces a beat signal. To avoid overlap of the beat signals in frequency domain, the two combs need to have a slightly different line spacing. The frequency of nth line in the signal comb spectrum is described by $f_s = f_r n + f_1$, where f_r is called the repetition rate, and f_1 is the frequency of the first line. The nth line of the LO comb should then be $f_{lo} = (f_r + \Delta f_r)n + f_1$, where Δf_r is the difference in the repetition rate. The beat signal is then produced at the frequency $f_{rf} = f_{lo} - f_s = \Delta f_r n$, forming a frequency comb in the radio frequency (RF) domain. The RF comb can be easily measured with RF electronics. The procedure is illustrated in Figure 3.3 in a symmetric dual-comb mode, in which both the signal and LO comb passes through the gas sample. Values for f_r and Δf_r can vary significantly depending on the application. In high resolution spectroscopy, most commonly $f_r \sim 100\,\text{MHz}$ and Δf_r is between 100 Hz and 1 kHz. The time required to measure a dual-comb spectrum at f_r optical resolution is the inverse of Δf_r, making dual-comb spectrometers fast compared to FTIR. Compared to grating spectrometers, a dual-comb offers much higher resolution.

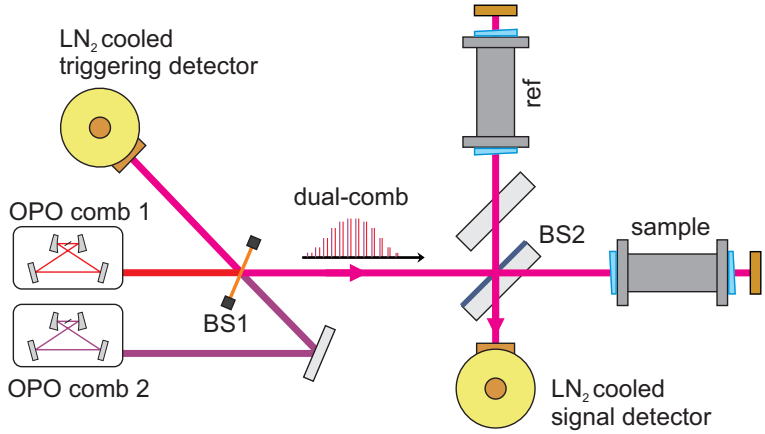

Figure 3.4: Outline of the experimental setup for validation of the presented BF method. BS: beamsplitter.

3.3 Experimental results

This section summarises the results of Article **II**, in which we demonstrated the first broadband background-free absorption spectroscopy with an interferometric background suppression. The experimental setup is outlined in Figure 3.4, and fully reported in Article **II**. The constructed interferometer follows the design laid in Figure 3.2, with the exception that the first surface of the beamsplitter (Thorlabs BSW511) had a broadband partially reflective dielectric coating to increase the reflection of the CaF_2 substrate to approximately 50 %. A rough estimate of the performance of the interferometer can be found by calculating the extinction ratio by considering intensity imbalance ρ arising from the optical components on the beam path. Using the manufacturer's data on the beamsplitter reflectance and transmittance, together with Fresnel coefficients for CaF_2, we found the expected extinction ratio over the range of the beamsplitter coating (1–6 µm) to be approximately $\Delta_P = 1 \times 10^{-4}$. The imbalance in ρ arose from an uneven number of Fresnel reflections between the two optical paths. Still, for the calculated extinction ratio, the expected noise equivalent absorbance was good, below 1×10^{-4} with a sufficient laser power. For the approximation of Δ_P, we neglected the phase imbalance from, for example, imperfect dispersion compensation that would in practise worsen the extinction ratio.

For experimental validation of the designed and constructed interferometer, we carried out experiments using a mid-infrared dual-comb spectrometer. The state-of-the-art dual-comb spectrometer consisted of two OPOs, which were coherently combined on a pellicle beamsplitter, producing two output beams. The spectrometer covered the spectral range from 1840 to 3180 cm^{-1}, at the $f_r = 115$ MHz (0.0038 cm^{-1}) spectral resolution. The normalised noise-equivalent absorbance was 0.027 $Hz^{-1/2}$ for a normal transmission measurement [48]. The experimental BF configuration required the use of two liquid nitrogen cooled detectors. The purpose of the first detector was to detect the light after the optical background suppression. The second detected the light without the suppression, which provided a triggering signal for the data acquisi-

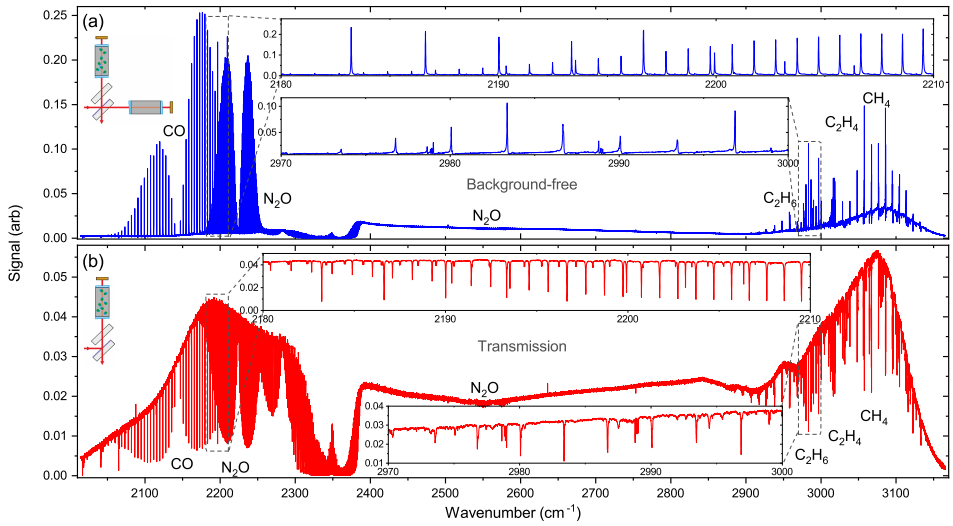

Figure 3.5: Raw data of dual-comb measurements in (a) BF-mode and (b) in TR-mode. The insets show close-ups of the spectra and the interferometer configurations.

tion. The triggering signal from the suppressed output would have been too imprecise because of its low optical power level. In addition to the dual-comb experiments, the suppression interferometer was tested with an FTIR at 0.125 cm^{-1} resolution using a different mid-infrared optical frequency comb light source spanning from 2.3 to 4.8 µm [49]. The results were similar to those obtained with the dual-comb spectrometer and are not reported.

Figures 3.5 and 3.6 show a collection of results from the experiments with the dual-comb spectrometer. In the measurements, the 'SAMPLE'-cell was filled with a mixture of five gases in the following volume mixing ratios: CO (0.25%), C_2H_4 (0.35%), C_2H_6 (0.2%), CH_4 (0.22%), and N_2O (0.12%) in N_2 at 120 mbar total pressure. The 'REF'-cell was evacuated. One measurement was taken in transmission mode (TR-mode) by blocking the reference arm of the interferometer, as illustrated in the inset of Figure 3.5 b). The other measurement was taken in the background-free mode (BF-mode) with the background suppression interferometer operational. In the transmission measurement, the optical power was also attenuated by a factor of 10 in order to avoid detector saturation, while the full combined laser power of 7 mW was used in the BF-mode. One can observe from Figure 3.5 that the peaks in the BF measurement are taller signalling a better SNR. At the same time, some interfering atmospheric lines from, for example $^{13}CO_2$ around 2250 cm^{-1} are missing since they were not present in the sample. This demonstrates another benefit of the BF technique.

For a closer performance evaluation of the background suppression interferometer, the data in Figure 3.5 were analysed to extract the imbalance factors ρ and ϕ as described in Section 3.1. The two variables are heavily cross coupled with both affecting the residual background level. The separation of the variables is possible in case absorption lines are present, since only ϕ affects the symmetry of the absorption peaks. With the help of HITRAN spectral database [28], we performed fitting of ρ and ϕ at

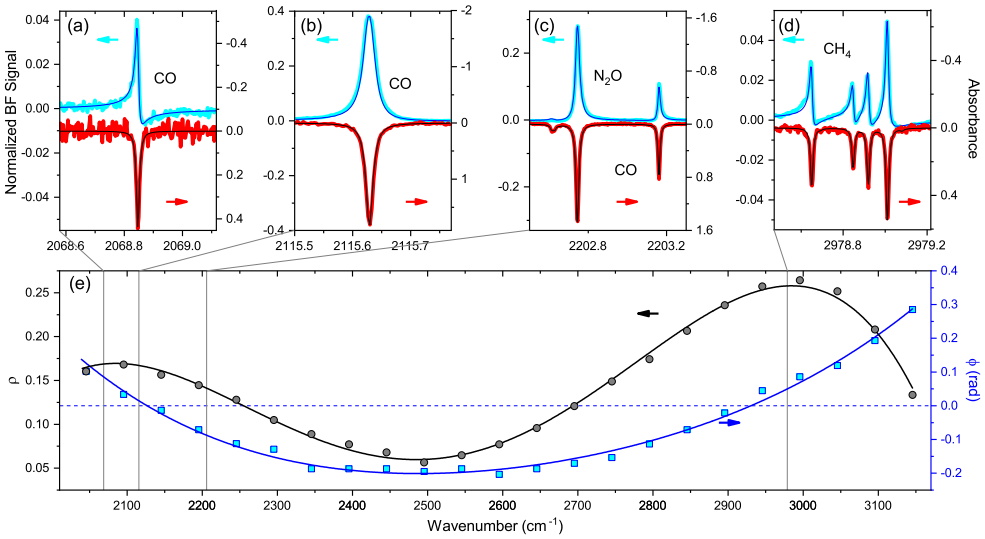

Figure 3.6: (a)-(d) Pointing up: zoom-ins of the data in Figure 3.5 (a). Pointing down: calculated absorbance from the data in Figure 3.5 (b). The thick lines show the measured data and the thin lines indicate the simulated spectra. (e) The best fitted values for the imbalance factors ρ (intensity) and ϕ (phase). The sparsely sampled data are fitted by fourth order polynomials (solid lines).

discrete points of the experimental spectrum with $50\,\mathrm{cm}^{-1}$ spacing. The coarse map of the imbalance factors was then fitted with fourth order polynomials. The result is shown in Figure 3.6 among a few example spectral lines in the BF and in TR-mode. The examples in figures 3.6 a)-d) also show the effect of ϕ on the shape of the lines. The shapes can be understood if the imaginary part b of the absorption line is included in approximation Equation 3.4, and recalling the shape of b from Figure 2.2 b). The approximation for the BF-signal is then written as $P_{bf} \approx \frac{P_0}{4}(b^2+2b\phi+\phi^2+\rho^2+2\rho a+a^2)$. The term b^2 is symmetric with the line centre and will symmetrically broaden the line in the measurement. On the other hand, the linear term $b\phi$ for non-zero ϕ creates an asymmetry to the measured line shape. According to the cosine function in Equation 3.6, the lines are skewed to the right (figures 3.6 a) and 3.6 d)) and left (Figure 3.6 c)), for positive and negative ϕ, respectively. Close to $\phi = 0$, the line appears symmetric (Figure 3.6 b)), although slightly broadened by the absorption related dispersion. At $\phi = \pi/2$, the peaks would appear equally tall on top and below the baseline, resembling the dispersion profile of the line as in Figure 2.2 b).

The example lines in figures 3.6 a)-d) give an idea of the SNR improvement by the BF-mode. For all the examples, the background suppression method gives a 2-4 times higher SNR than the transmission measurement, even though the available optical power was limited. With a high power frequency comb, the SNR and NEA are expected to improve considerably even with the current implementation of background suppression interferometer. For example, watt-level MIR frequency combs have been reported in Article **2** and by other groups [50–52].

Chapter 4

Cantilever-enhanced photo-acoustic spectroscopy

Photo-acoustic spectroscopy is an indirect method of measuring absorption: it measures a change in the state of the gas. It is an intrinsically background-free technique, meaning that without absorption no photo-acoustic signal is generated. In the photo-acoustic (PA) effect the energy of the absorbed light is dissipated non-radiatively as heat. Increase in the gas temperature creates a local increase in pressure. The excitation source is modulated periodically in such way that the absorption becomes periodic producing an acoustic wave, which can be measured with a sensitive microphone. Possible modulating techniques include optical power modulation and wavelength modulation. The photo-acoustic effect was first discovered by Alexander Graham Bell in 1880 [53]. The potential of photo-acoustics as a spectroscopic tool was discovered much later after sufficient development in microphone and light source technologies. In the mid 20th century, especially after the invention of laser, the PA effect started to gain wider interest as a spectroscopic method [54]. Since then, photo-acoustic spectroscopy has been applied to analyse solid, liquid, and gaseous samples [7].

The basic photo-acoustic measurement system for detection of trace gases is simple. It comprises a light source and its modulator plus a sample cell equipped with a microphone for PA-signal detection. The cell has windows for the light to pass through, and is generally accompanied with hardware for signal processing and gas handling. The magnitude of the PA-signal response S can be generally expressed in millivolts as [55]

$$S = S_m P C_{cell} N_0 c_m \sigma \tag{4.1}$$

where S_m is the microphone sensitivity (mV/Pa), P is the optical power of the incident light (W), C_{cell} is the PA cell response constant (Pa/cm^{-1}), N_0 is the total number density of molecules (molecule/cm^3), c_m is the volume mixing ratio of the target gas, and σ is the absorption cross section (cm^{-1}). In order to measure as small c_m as possible, one must maximise the other factors in the equation. It should be noted that this model is simplified in a sense that it does not include the non-radiative decay effects, which may increase or decrease the strength of the PA signal in the case of some molecules gas matrices [56, 57]. This, together with the fact that it is difficult to

obtain accurate theoretical prediction for the $S_m C_{cell}$ product, leads to the need for each PA detector to be calibrated. This is a common drawback of indirect absorption spectroscopic methods, as compared to direct laser absorption spectroscopy, which can provide absolute absorption measurements without calibration.

The absorption cross section σ is a molecule specific wavelength dependent quantity, equal to $S_0(T)f(\nu, \nu_0\ , T, p)$ of Equation 2.1. The cross section maybe maximised by a suitable choice of wavelength, which depends on the absorption spectrum of the molecule. Usually the electronic transitions from the visible to ultraviolet range are the strongest. However, this region is associated with technical problems such as lack of suitable light sources and poor selectivity due to the lack of resolvable fine structure in the spectra. The mid-infrared region, on the other hand, has a rich and better resolved spectrum of strong fundamental rotational-vibrational transitions, which makes it highly preferred for spectroscopic trace gas detection. A major advantage of photo-acoustic detection is that the operation wavelength can be chosen freely as opposed to photodetectors, which work only at a certain wavelength range.

The factor $N_0 c_m$, equal to the total number density of absorbing molecules, states that the PA-signal is directly proportional to the sample concentration. This is the basis for quantitative trace gas detection, in which the interest is usually in the volume mixing ratio of the analyte. The cell constant C_{cell} describes the acoustic profile of the PA cell. In some cases, one may design the PA cell to have an acoustic resonance for the detection frequency in order to enhance the PA-signal response [58, 59]. In that case, the PAS is referred to work in a resonant mode as opposed to a non-resonant mode of operation, in which the acoustical signal frequency is clearly lower than the lowest resonance frequency of the cell. The term P indicates that higher optical power results directly in a stronger PA-signal, which is why monochromatic lasers are especially useful for PAS. This is also the approach used in the articles **I** and **III** to improve the PA detection limits.

The choice of a microphone is naturally paramount for photo-acoustic detection. The smaller the change of pressure that the microphone can detect, the better it will perform in PA spectroscopy. The fundamental limit for microphone performance is set by the thermal motion of the gas molecules. The moving molecules bombard the microphone, creating a noise floor with Brownian characteristics. This limit has been reach by some cantilever microphones which are somewhat similar to those used in, for example, atomic force microscopy [60, 61]. In addition to the microphone sensitivity S_m, one must consider the acoustic frequency response of the microphone. For example, at high frequencies in the kHz to MHz range, the non-radiative relaxation times of the molecules may become a limiting factor resulting in a phase shift and fading of the PA-signal [54]. There are mainly three types of microphones applied in modern high performance PAS: ordinary capacitor-based microphones, quartz tuning forks in quartz tuning fork enhanced photo-acoustic spectroscopy (QEPAS) [15, 62], and silicon cantilevers in cantilever-enhanced photo-acoustic spectroscopy (CEPAS) [60, 63–67]. Of the three, ordinary microphones and quartz tuning forks operate in the kHz range. They are the most affordable and easily available, but lose in detection sensitivity by at least one to two or more orders of magnitude compared to the most advanced cantilever-based microphones [68]. QEPAS and CEPAS are inventions of the 21th century. Currently, most of the new research on PA trace gas detection focuses in these two techniques.

In this thesis, I focus on the application of CEPAS to trace gas detection. The microphone and PA detection module is manufactured by Gasera Ltd., who base their technology on the work by J. Kauppinen et. al. [69]. The operation principle of the microphone and the PA detection module is briefly summarised here, although their development was not part of the thesis. The cantilever is a piece of silicon that is 5 mm long, 1 mm wide, 10 µm thick and separated from its frame by a 3 µm wide gap on three sides. The long end of the cantilever can moving freely so that in a PA experiment, the tip of the cantilever is easily deflected by the pressure wave. The deflection is measured by a compact laser interferometer down to 1×10^{-12} m level and with at least five orders of magnitude linear dynamic range. The acoustic modulation/measurement frequency is typically chosen in 10–100 Hz range, which is well below the first resonance frequency (∼500 Hz) of the cantilever, as well as well below the acoustic resonance of the PA cell. The non-resonant operation has been found to result in the best signal-to-noise ratio and reliability [68].

A useful figure of merit for PA trace gas detectors is the normalised noise-equivalent absorption (NNEA):

$$\mathrm{NNEA} = \alpha_{min} P_0 \sqrt{t} \tag{4.2}$$

where P_0 is the incident optical power, and α_{min} is the noise equivalent absorption coefficient (refer to Equation 2.1) for integration time t, which is the inverse of two times the detection bandwidth. The NNEA is commonly used for direct performance comparison among different PA trace gas detectors. However, in some cases, it may be misleading as the most appropriate figure of merit for trace gas detection is the limit of detection (LOD). As an example, the NNEA does not take into account the absorption strength of the molecule, or the possible difference in the PA response of different gases and matrices. There exists also some discrepancy on determining α_{min}. For example, some consider only the intrinsic detector noise whereas others also include fluctuations from the sampling system. For the CEPAS module used in this work, the NNEA value is as low as in the order of $1 \times 10^{-10}\,\mathrm{Wcm^{-1}Hz^{-1/2}}$ [68]. For comparison, typical values for other techniques, such as QEPAS, are in the order of 1×10^{-8}–$1 \times 10^{-9}\,\mathrm{Wcm^{-1}Hz^{-1/2}}$ or worse [15,70]. In Article **I**, instead of the NNEA, we show a comparison of the best reported noise equivalent concentrations for PAS to highlight the relevance of the actual detection performance.

The CEPAS cell used in this thesis consists of two chambers separated by the cantilever as illustrated in Figure 4.1. The long chamber at the top in the figure was for the actual PA measurement and the the lower one for balancing low frequency acceleration noise imposed on the cantilever [16]. The chambers were connected by two out of the plane channels. The measurement chamber was 10 cm long and 4 mm in diameter with windows at both ends for the light to pass through. The total volume of the CEPAS cell was 11 ml. The readout interferometer was placed outside of the gas cell, with a window providing optical access to the cantilever. The gas in the cell could be exchanged using three valves, two at each end of the measurement chamber, and one at the back of the balance chamber. In a typical gas exchange routine, the sample flowed through the cell from both ends of the measurement chamber to the balance cell. Under a pressure difference, the cantilever bends considerably so that the exchange is efficient even though the initial gap around the cantilever remains small. For a PA measurement, the valves are closed because a gas flow through the cantilever

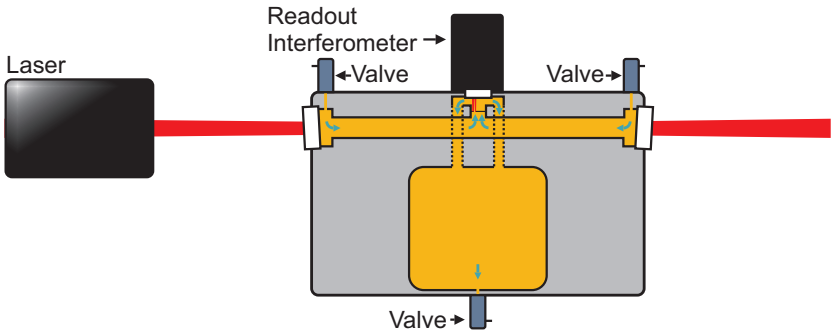

Figure 4.1: Illustration of the two chamber structure of the CEPAS cell and its typical gas flow path marked with blue arrows.

creates intolerable noise to the detection.

4.1 Use of high optical power in photo-acoustic spectroscopy

The strength of a photo-acoustic signal is directly proportional to optical power, thus favouring the use of high power lasers. The power P in Equation 4.1 is also the factor that is most conveniently improved. In this section, we investigate two possible realisations for high optical power in a PA measurement. In the first realisation, which is discussed Article **I**, an optical parametric oscillator (OPO) is used to convert the light of a high-power near-infrared light source to the mid-infrared, in order to access the strong fundamental transitions that lie there. The approach is straightforward and excludes any technical challenges other than the construction of the OPO. However, the OPO is bulky and sensitive to mechanical disturbances. As it is, the development of the system to a portable instrument could be challenging. In fact, most realisations of tunable high power laser systems are unsuitable for portable instruments. In addition, some wavelength regions of the mid-infrared spectrum may be challenging to reach with such technology. In the second realisation, presented in Article **III**, we develop a more general approach that is not limited to laboratory use. The approach is based on an optical build-up cavity to accumulate the power of a low-power laser inside the PA cell. The technique is applicable to various small and robust lasers, such as near-infrared DFB lasers or QCLs.

4.1.1 Use of an optical parametric oscillator

An optical parametric oscillator coherently converts a beam of laser light at high optical frequency, called the pump, to two beams at lower optical frequencies, called the idler and the signal. An optical parametric oscillator bears resemblance to a laser in that they both feature an optical resonator embedded with a gain medium. Optical resonators are discussed in more detail in Section 4.1.2. However, instead of stimulated emission, the gain in an OPO is based on a nonlinear optical process called optical

parametric amplification (OPA). In the OPA an optical wave at the frequency ω_p interacts with another wave at the frequency ω_s so that the power at the wave ω_s is coherently amplified. In this process, a third wave at the frequency $\omega_i = \omega_p - \omega_s$ is also generated. The designations here are as the pump (p), signal (s), and idler (i), listed in the order of decreasing optical frequency. The OPA process can be exploited in different ways. In case ω_i is the beam of interest and both ω_p and ω_s are provided as an input, the process is called the difference frequency generation (DFG). In case only ω_p is provided as an input, the ω_i and ω_s waves are generated from quantum fluctuations of the vacuum, and the process is called the optical parametric generation (OPG). OPG is the process that seeds the generation of the idler and signal in an OPO, which are then further amplified by OPA and DFG.

OPA, DFG and OPG are categorised as three-wave mixing processes, also known as parametric interaction processes, which are based on second order nonlinear optics. They can take place in a dielectric medium at high optical intensities, provided that the second order electric susceptibility $\chi^{(2)}$ of the medium is non-negligible. Electric susceptibility is a parameter that embodies the dielectric properties of the medium. It is defined through the relation between an electric field E and the induced polarisation density P as [71]

$$P = \epsilon_0 \chi^{(1)} E + \epsilon_0 \chi^{(2)} E^2 + \epsilon_0 \chi^{(3)} E^3 + ... \tag{4.3}$$

where ϵ_0 is the electric permittivity of vacuum. The first term is referred to as the linear susceptibility, which dominates in most cases. The higher order terms $\chi^{(n)}, n \geq 2$ are referred to as nonlinear susceptibilities, which vanish quickly as the order increases. In most cases, the higher order terms can be neglected. In general, $\chi^{(n)}$ are $n+1$ rank tensors, and P and E are vector quantities. Here, we shall treat them as scalars for simplicity. The simplification can be understood as the incident and induced light having linear polarisation. Considering only the second order term, the emergence of parametric processes is found by looking at interaction of the pump and signal beams written in the form of two monochromatic electric fields as $E_s(t) = E_0 \cos(\omega_s t)$ and $E_p(t) = E_0 \cos(\omega_p t)$ taken at time, phase and propagation distance zero. The second term in Equation 4.3 then becomes

$$\begin{aligned} P^{(2)} &= \epsilon_o \chi^{(2)} E_0^2 \left[\cos(\omega_p t) + \cos(\omega_s t)\right]^2 \\ &= \epsilon_o \chi^{(2)} E_0^2 [1+ \\ &\qquad + \frac{1}{2}\cos(2\omega_p t) \\ &\qquad + \frac{1}{2}\cos(2\omega_s t) \\ &\qquad + \cos\left((\omega_p + \omega_s)t\right) \\ &\qquad + \cos\left((\omega_p - \omega_s)t\right)]. \end{aligned} \tag{4.4}$$

In addition to recognising the DFG as the last term in Equation 4.4, there is a sum frequency term $\omega_p + \omega_s$, second harmonic generation terms $2\omega_s$ and $2\omega_p$, and a constant term corresponding to an effect known as optical rectification.

For an efficient parametric process to take place, two conditions need to be met: conservation of energy (Equation 4.5) and momentum (Equation 4.6)

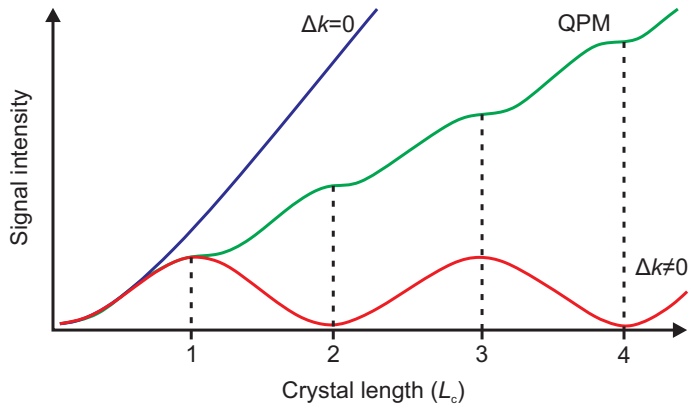

Figure 4.2: Effect of phase matching on the growth of three-wave mixing signal intensity in the case of perfect phase matching ($\Delta k = 0$), quasi phase matching (QPM), and phase mismatch ($\Delta k \neq 0$).

$$\omega_p = \omega_s + \omega_i \tag{4.5}$$

$$k_p = k_s + k_i + 2\pi/\Lambda \tag{4.6}$$

where $k_j = n_j\omega_j/c$ is the wave vector, with n_j being the refractive index and c being the speed of light in vacuum. The process of fulfilling the conservation of momentum is called phase matching. In Equation 4.6 we have directly adopted a popular scheme for quasi phase matching (QPM) [72] by adding the term $2\pi/\Lambda$, where Λ is a material parameter described later in the text. The QPM scheme is helpful in achieving an efficient parametric process because the exact phase matching condition is in general difficult to satisfy due to the wavelength dependence of the refractive index n_j, known as dispersion. Consider the case of phase mismatch $\Delta k = k_p - (k_s - k_i)$, in which the pump, signal and idler waves travel at different velocities in the medium. After a propagation distance of $L_c = \pi/\Delta k$, known as the coherence length, the waves start to interfere destructively converting energy back to the pump beam. The process continues, altering between destructive and constructive interference as illustrated in Figure 4.2. Because the conversion of energy after one L_c is typically weak, it is desirable to continue the process over many L_c. In QPM, the orientation of the crystal structure of the medium is reversed at every L_c so that the parametric process continues constructive throughout the crystal (Figure 4.2). The period, over which the crystal structure repeats itself is called the domain width and is denoted by $\Lambda = 2L_c$. The domain width is typically in the range of 10–100 µm. With a nonlinear crystal length in the order of cm, the nonlinear conversion efficiency can be ten to hundreds of times higher with QPM than without phase matching over single L_c. For some birefringent materials it is possible to obtain phase matching without QPM, by properly orienting the polarisation and the propagation direction of the pump beam with respect to the crystal structure of the medium (Figure 4.2). This approach gives the highest nonlinear conversion efficiency but is also the most difficult to implement.

The most important material for OPOs and QPM is lithium niobate ($LiNbO_3$). It

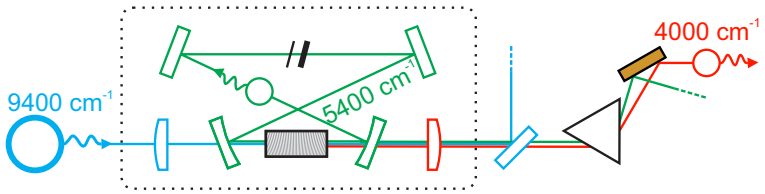

Figure 4.3: A typical singly resonant OPO, which is configured as used in the experiments of Article **I**. A high energy pump photon (blue) enters a ring cavity equipped with a nonlinear crystal and two etalons. The photon splits in two lower energy photons: the signal that resonates in the cavity (green), and the idler that directly exits the cavity (red). Residuals of the pump and signal beams are filtered out with a dichroic mirror and an equilateral prism, respectively.

has a large nonlinear coefficient and a transmission range of 0.33–5.5 µm, which suits well the generation of mid-infrared light in the 2–4 µm range via parametric down conversion. $LiNbO_3$ is a ferroelectric crystal, which can have its crystal structure permanently reoriented in a strong electric field. The effect is useful for preparing a QPM structure in a process called periodical poling, in which case the name of the periodically poled $LiNbO_3$ is abbreviated PPLN. Often $LiNbO_3$ is further doped with MgO to improve its damage threshold against high intensity optical fields [73]. Other popular materials that are suitable for QPM with transmission in visible to 5 µm range include lithium tantalite ($LiTaO_3$) and potassium titanyl phosphate (KTP). For longer wavelengths, GaAs with transmission range of 0.9–17 µm is a popular choice [21, 74].

In an OPO, the nonlinear crystal is placed in the focus of an optical cavity. The cavity mirrors are highly reflective for the signal wave, and transmissive for the idler and the pump. This is the case of a singly resonant OPO, whereas a doubly resonant OPO has mirrors that are highly reflective for both the signal and idler beams. When a sufficiently high intensity pump beam is coupled in the crystal, it will spontaneously generate signal and idler photons from quantum noise through OPG. The wavelengths at which the signal and idler are amplified depend on the phase matching conditions, as well as the resonance modes and optical losses of the cavity. Considering the case of a singly resonant OPO, the optical cavity provides feedback for the signal wave so that it starts to build up in the cavity through OPA. As there are then both strong pump and signal beams present, a strong idler beam is also generated. The mid-infrared idler beam is coupled out of the cavity to be used in an experiment.

Tuning of the idler wavelength can be performed in many ways. The fastest and most accurate way for high resolution spectroscopy is to tune the pump wavelength. The idler wavelength follows the pump wavelength tuning according to Equation 4.5, as the signal wavelength is fixed to the cavity resonance. For a coarse tuning, the phase matching condition may be altered by changing the temperature or the poling period of the nonlinear crystal. In addition, some control of the signal wavelength is possible by tuning the cavity losses by, for example, placing and rotating an etalon in the cavity. The bandpass-filter-like transmission profile of an etalon is also often useful for improving the single-mode operation of the OPO [75, 76].

Figure 4.3 shows schematic of the OPO used in the experiments of Article **I**. The OPO was configured in a way typical for a singly resonant continuous-wave (CW)

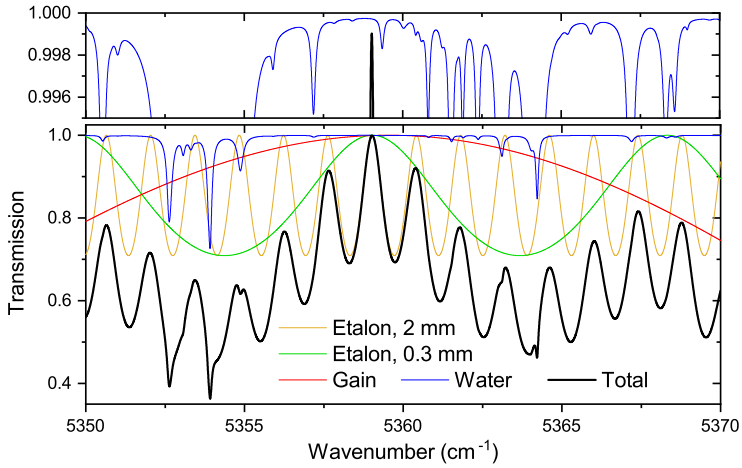

Figure 4.4: Simulated OPO cavity transmission for the signal wavelength.

OPO. The optical cavity was a bow-tie ring resonator, in which the oscillating signal beam propagates only in one direction. The pump laser was a continuous wave DFB operating at 1064 nm, which was amplified up to 20 W of optical power with an ytterbium fibre amplifier. The MgO-doped PPLN nonlinear crystal had a periodically poled QPM structure in a fanout pattern with Λ in the range of 26.5–32.5 µm. The poling period and the PPLN temperature was adjusted such that an idler wave was generated at 2476 nm, which targeted a strong ro-vibrational transition of hydrogen fluoride (HF). The OPO had two YAG etalons of 0.3 mm and 2 mm in thickness to control the cavity losses and to improve single-mode operation. The etalons were placed in the secondary focus of the cavity. Residuals of the pump and signal beams were filtered from the output of the OPO with the help of a dichroic mirror and an equilateral prism.

For the experiment, it was crucial that the OPO operated stable at high idler power without mode hops for a long period of time. For this reason, special attention was paid to allow only a single low loss cavity mode to resonate. Figure 4.4 shows a simulated transmission spectrum of the cavity round trip, where we have included the transmission of the two etalons, water absorption, and the unity normalised gain bandwidth of the nonlinear crystal. The cavity resonance modes were not included because of their fine spacing (0.01 cm^{-1}) compared to other features. The water transmission was calculated using the HITRAN database [28] for 0.22 % water volume mixing ratio, 1 m path length, and standard temperature and pressure. The figure shows that the design would allow single-mode operation at a wavelength with low atmospheric absorption losses, provided that the two etalons were correctly aligned. In this configuration, the OPO ran continuously without mode hops for hours at 13 W pump power, at which it generated about 1 W of idler power. The performance of the OPO was typical in terms of optical output power, whereas the stability was excellent concerning the bit unusual operation quite close to degeneracy of the signal and idler wavelengths, where mode hops are usually difficult to avoid [77].

Photo-acoustic spectroscopy with a high power OPO

The OPO presented in figures 4.3 and 4.4 was used as a light source in Article **I**, where we performed a record level trace gas detection of HF by wavelength modulated cantilever-enhanced photo-acoustic spectroscopy. The purpose of the work was to demonstrate the high trace gas detection sensitivity that can be attained by CEPAS. In this particular case, we made use of the strong transitions of HF with a line intensity of $2.381 \times 10^{-18}\,\mathrm{cm}^{-1}/(\mathrm{molecule}\,\mathrm{cm}^{-2})$ at 4039 cm^{-1} [28], and the high output power of the constructed CW-OPO. The scheme is also applicable to detection of many other molecules with equal performance. The experimental configuration was simple. The idler beam of the OPO was aligned through the CEPAS cell in a double pass configuration. For a background-free photo-acoustic signal generation, the wavelength of idler beam was modulated at the 30 Hz rate. The phase sensitive detection by lock-in principle was performed at the second harmonic (60 Hz). In addition, the optical power and wavelength of the idler beam were monitored and used in normalisation of the PA-signal. Other experimental details, such as the optimisation of the modulation amplitude, are discussed in Article **I**.

Figure 4.5 summarises the spectroscopic results, which are fully reported in Article **I**. Figure 4.5 a) shows a second harmonic spectrum of the targeted HF line, measured at 97 ppt volume mixing ratio for identification of the HF peak. Because the spectral scan was slow, routine measurements were carried out by measuring only the peak of the spectral line. A single HF data point was recorded in 15 s. A point composed of a 9 s period for the gas exchange cycle and a 6 s period for recording the signal. Figure 4.5 b) shows a 200 min long continuous set of data recorded at low HF volume mixing ratio. The data was used to perform an Allan deviation analysis to determine the noise-equivalent concentration (NEC) of the system [78]. For a single 15 s measurement, the NEC was found to be 2.5 ppt. By averaging, the Allan plot predicts the NEC to be improved down to 0.65 ppt in 32 min.

The achieved NEC is the best reported so far for any CEPAS measurement, and among the few PAS experiments that have reached a low ppt to sub-ppt level NEC [9, 79]. Article **I** provides a wider comparison of the reported PA experiments with sub-ppb level NEC. Here, we restrict the discussion to the three best results, including our work, with about the same NNEA coefficients but somewhat different NECs due to other performance factors. In the work [79] by Peltola et al. the experimental configuration was quite similar to the one reported here. They used a similar CEPAS detector and an intensity modulated 4.7 W CW laser at 532 nm to achieve a 50 ppt NEC in the detection of NO_2 using an electronic transition. The lower NEC compared to Article **I** was mainly due to weaker absorption cross section of NO_2. In another PAS work by Xiong et al. [9] an NEC of 0.75 ppt was reported in the detection of SF_6 for a rather special experimental scenario. They employed a 1 W CO_2 laser at 10.6 µm together with two acousto-optic modulators for frequency shifting to produce a moving intensity modulation pattern inside the PA cell for acoustic signal generation. The on-resonance PA-signal was read piezoelectrically, similarly to QEPAS, by a specially fabricated α-BiB_3O_6 crystal with a resonance frequency around 443 kHz. In addition, the PA-signal response was enhanced by an order of magnitude by measuring the SF_6 in argon buffer gas instead of a real-world gas matrix, such as air. Lastly, it is worth mentioning that in general a low-ppt and sub-ppt level NEC in LAS is uncommon. To my best knowledge, the only other LAS based detection technique to achieve sub-ppt

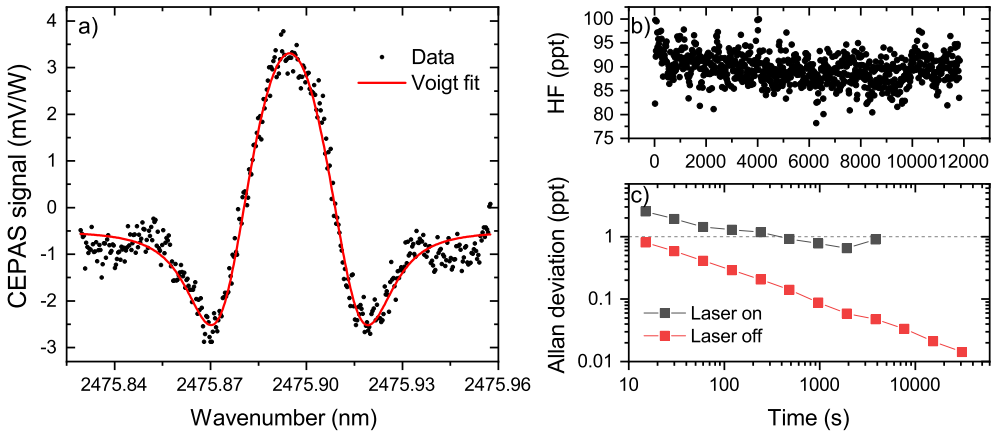

Figure 4.5: (a) Measured second harmonic spectrum of 97 ppt of HF in dry air. The red trace is the second harmonic signal of a Voigt profile fitted to the data. (b) A long continuous measurement of HF at a low volume mixing ratio. (c) Allan deviation of the data in (b) and a data set recorded with the laser turned off.

level detection limits is saturated absorption cavity ring down spectroscopy [8].

The demonstrated highly sensitive trace gas detection using CEPAS still has room for improvement. The achieved NEC was limited by experimental factors other than the detector noise. The difference is evident by comparing the 'laser on' and 'laser off' traces in Figure 4.5 c). The 'laser off'-case shows the intrinsic detector noise limit, which is three times lower than the actual HF measurement noise, reaching the sub-ppt level NEC already for a single 15 s measurement. The excess noise is presumed to origin most dominantly from noise in the optical power of the light source, and from actual fluctuations in the HF concentration. The low HF concentration was produced by desorption from the HF enriched surfaces in the gas line. The desorption rate depended strongly on the humidity of the carrier gas, which was dry air from the pressure line of the building. The humidity of the air varied by a few percent over the course of the measurement.

4.1.2 Use of an optical build-up cavity

Optical cavities, also called resonators, are a common element in optical and laser physics as well as in laser spectroscopy. An optical cavity is formed by an arrangement of optical components, such as mirrors, which allow light to circulate [20]. Constructive interference of successive cycles allows the optical intensity in the cavity to grow high, and the photons to travel a long distance before exiting the cavity. In physics, the cavities are mostly used to accumulate optical power for nonlinear interactions and to provide optical feedback. In spectroscopy, they are mostly used to increase the interaction path length in various cavity-enhanced spectroscopic techniques, such as cavity ring-down spectroscopy and cavity-enhanced absorption spectroscopy [80]. Sometimes, an optical cavity is called a Fabry-Perot interferometer, and is used as a high resolution optical filter for spectrometry, as an example. This application exploits

the fact that transmission spectrum of an optical cavity exhibits a series of equidistant sharp peaks.

In photo-acoustics, the PA-signal scales linearly with optical power. Therefore, the signal can be enhanced by placing the PA detection system in an optical cavity. The cavity is referred to as an optical build-up cavity in case it does not contain an optical amplification medium. In the literature, there are a few reports on improving the photo-acoustic detection performance by an optical build-up cavity [70, 81–86]. In these articles, the power build-up factor (BUF), by which the cavity amplifies the incident optical power, ranged from one hundred to few hundreds. The higher the BUF, the more complex and challenging it is to couple the laser light into the cavity. Our work in Article **III** was the first based on CEPAS and the first to employ wavelength modulation for PA-signal generation instead of amplitude modulation.

An efficient coupling of a laser to an optical build-up cavity requires attention on the cavity design, control of the laser wavelength, as well as focusing of the laser beam into the cavity [80, 87]. The requirement for proper focusing of the laser beam to the cavity is to match the size and location of the beam waist to that of the resonance mode of the cavity. The process is known as mode matching. In most cases, including this thesis, the laser is coupled to the fundamental Gaussian mode. With given initial Gaussian beam parameters and geometry of the cavity, the required relay optics for mode matching can be designed conveniently by, for example, with the help of ABCD-matrix formalism for Gaussian beam propagation [88]. In practise, the relay optics would comprise an arrangement of lenses and/or curved mirrors. If the beam parameters are unknown, they can be measured by the use of a beam profiling camera or the knife edge technique [89, 90], as an example.

Further steps in the design of an efficient coupling of a laser to an optical build-up cavity requires a closer description of the properties of optical cavities. Let us consider a two mirror linear cavity, as used in the experiments of Article **III**, with a round-trip length of L_r. The fundamental Gaussian modes of the resonator will occur every free spectral range (FSR), which is expressed as FSR$=c/L_r$, where c is the speed of light. The modes allow resonance over a certain spectral band, known as the linewidth $\Delta\nu_c$ of the cavity, with a shape well approximated by a Lorentzian function, similar to Equation 2.3. The linewidth is related to the FSR by a parameter called finesse (F) by $F = \mathrm{FSR}/\Delta\nu_c$, which can be written as

$$F = \pi \frac{[R(1-A_c)]^{1/4}}{1-[R(1-A_c)]^{1/2}} \approx \frac{\pi}{1-[R(1-A_c)]^{1/2}}. \tag{4.7}$$

Equation 4.7 shows that the finesse is fully defined by the total cavity round-trip losses $1-[R(1-A_c)]^{1/2}$, where R is the power reflectivity of the front mirror, and A_c is the power attenuation coefficient for all other round-trip cavity losses, such as gas absorption, losses on intracavity components and transmission of the end mirror [91]. The finesse approaches infinity in the case of a lossless cavity: $R(1-A_c) \to 1$.

The achievable build-up factor BUF, defined as the ratio of resonating optical power to the incident power, is found to be

$$\mathrm{BUF} = \frac{1-R}{[1-\sqrt{R(1-A_c)}]^2} \tag{4.8}$$

where the front mirror was assumed lossless, meaning that the sum of reflectance and transmittance of the mirror equals one ($R + T = 1$). Equation 4.8 has its maximum $\mathrm{BUF}_{\max} = 1/T \approx F/\pi$ in the so-called impedance matched case where $R = 1 - A_c$. The impedance matched condition means that the coupling losses of the front mirror equal other round-trip losses of the cavity [91]. If the transmission of the end mirror is accurately known, the intracavity power and the BUF can be determined experimentally by measuring the transmitted optical power on resonance. A more direct way to measure the intracavity power is to record the PA-signal with and without the build-up cavity as the PA-signal is directly proportional to the optical power and hence, grows directly with the BUF.

If the spectral linewidth of the laser $\Delta\nu_l$ is larger than that of the cavity, the coupling of the light in the cavity is reduced by approximately a factor of $\Delta\nu_c/\Delta\nu_l$ [80]. This is a profound problem in achieving a high BUF with a standard semiconductor laser, which has a linewidth in the order of MHz. An impedance matched build-up cavity with a linewidth of 5 MHz would have a BUF of 100, assuming an about 10 cm long cavity. It is useful to notice that a shorter cavity has a broader linewidth for the same BUF as a longer one, thus favouring the use of short cavities. The coupling efficiency to a high finesse cavity can be improved by the use of high bandwidth locking electronics in the so called Pound-Drever-Hall (PDH) locking scheme [92]. Due to technological constraints, the PDH locking is mostly suited for near-infrared lasers. In the mid-infrared region, a solution is to use optical feedback in locking the laser to the cavity and possibly narrowing the linewidth [83, 86]. Both methods increase the complexity of the setup considerably compared to a dither-and-lock method, in which the laser frequency is dithered around the cavity modes or-vice-versa for a generation of a locking signal.

The dither-and-lock method resembles the 1st harmonic detection in wavelength modulation spectroscopy, introduced in Chapter 2. The locking procedure is illustrated in Figure 4.7 for the experimental setup in our work. The laser frequency (red traces) was slightly modulated at 5 MHz rate by feeding a sinusoidal voltage signal from a signal generator (local oscillator, LO) directly to the laser anode through a bias-T. Analogous to the WMS method described in Chapter 2, the frequency modulation produced an amplitude modulated transmission signal at the output of the cavity (blue traces), as the laser frequency was dithered around a cavity resonance. The signal contains harmonics of the LO frequency at different amplitudes, depending on the location around the cavity resonance mode (compare the two examples at the centre of the cavity mode, and on the slope). Next, the transmission signal was demodulated with a phase-controlled LO signal (P) and low-pass filtered for higher harmonic rejection (LP), equivalent to the lock-in detection in WMS. The resultant derivative shaped error signal was fed to a feedback-controller (PID), which outputs a control signal to the laser current driver. The specified maximum linewidth of the DFB laser used in our experiments was 5 MHz. Since this was less than the linewidth of our build-up cavity, the described dither-and-lock method with a slow feedback loop was sufficient to rigidly lock the laser frequency to the cavity mode.

In some cases, spectroscopic measurements with an optical build-up cavity may become nonlinear. Since Equation 4.8 depends on the losses of the cavity, including molecular absorption, the BUF is reduced in the presence of a strongly absorbing sample. For a cavity with a high BUF, the effect is more pronounced. Let us estimate

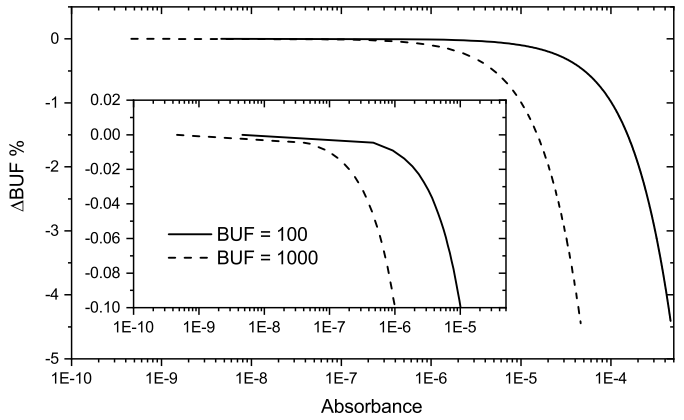

Figure 4.6: Relative change of the build-up factor as a function of cavity round-trip absorbance. The chosen absorbance range is the estimated dynamic range of the CEPAS detector with 10 mW input power and 1 s measurement time.

the magnitude of the effect in the case of the CEPAS sensor, used in the work of this thesis. The CEPAS has an NNEA of about $2 \times 10^{-10}\,\mathrm{Wcm^{-1}Hz^{-1/2}}$, a linear dynamic range of at least five orders of magnitude, and a 10 cm long PA-cell [16]. Assume that the laser has an output power of 10 mW, and the measurement time is 1 s. Recalling the equation for the NNEA (Equation 4.2), the detectable absorbance range is found to be from 2×10^{-7} to 2×10^{-2}. The use of a build-up cavity could lower the detection range by a factor of 100 to 1000, equal to the attainable BUF. Figure 4.6 shows a calculated relative change in the BUF as a function of round-trip absorbance in the cell. The lossless front and back mirror have reflection coefficients $R = 0.99$ and 0.999, in the case of BUF=100 and 1000, respectively. The calculations show a decline of a few percent in the upper end of the measurable absorbance range. Still, the lower end of the range provides three orders of magnitude measurement range with less than 0.1 % decline in the BUF. The decline can be considered negligible in most cases. If necessary, measurements can be corrected for the reduced BUF. In fact, the effect can be beneficial since it would increase the measurement range of the system as the strength of the signal is reduced at high concentrations and therefore the detector does not saturate as quickly.

Another nonlinear effect to consider with optical cavities is optical saturation of the probed molecular transition. If the intensity of the laser beam is high enough, such as at the focus of the cavity, it may reach the saturation intensity of the molecular transition. At saturation, the lower energy state of the transition becomes depleted, which is observed as reduction of absorption in a measurement. The saturation intensity depends on the strength and relaxation rate of the transition. It can be calculated or measured experimentally [86, 93].

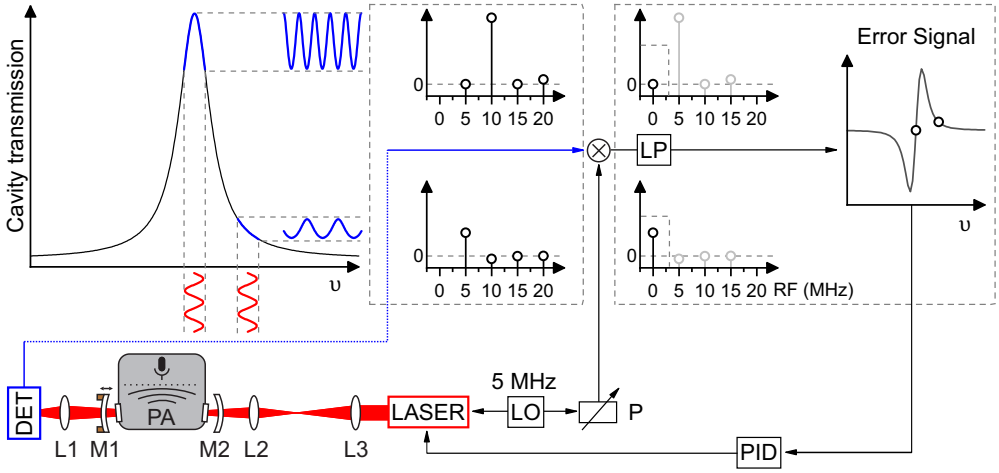

Figure 4.7: Process of locking the laser frequency to the cavity transmission peak via a dither-and-lock method. DET: photodetector, LP: low-pass filter, LO: local oscillator, P: phase control, PID: feedback-controller, L: lens, M: mirror, PA: photo-acoustic detector.

Cavity-enhanced cantilever-enhanced photo-acoustic spectroscopy

The build-up cavity in the experiments of Article **III** was designed for spectroscopy in the near-infrared region, which is rich in overtone bands of molecules. It is also convenient from the optical design perspective since technology for the near-infrared is mature and relatively inexpensive. The technical experimental arrangement is outlined in Figure 4.7, and described fully in Article **III**. The cavity consisted of two concave mirrors with reflective dielectric coatings for the operation wavelength of 1530 nm. The specified radius of curvature and reflectivity of the mirrors were 75 mm (97.5 %) and 100 mm (99.9 %) for the front and rear mirror, respectively. The front mirror had a lower reflectivity than the rear mirror to achieve a better impedance matching when the PA-cell was placed in the cavity. The cell had AR-coated windows which caused, according to specifications, a total round-trip loss of 0.56 % in the cavity. The spacing of the cavity mirrors was 150 mm, which resulted in 120 µm waist size for the fundamental Gaussian mode. The calculated and experimentally verified BUF was 100. With an available input power of 7.5 mW from a DFB laser, the maximum intracavity intensity was $0.33\,\mathrm{W mm^{-2}}$, which is well below the saturation intensity of most near-infrared transitions at typical pressures for trace gas detection. Moreover, reduction of the BUF due to intracavity absorption is expected to be small within the measurement range of the CEPAS detector.

In PAS, wavelength modulation is often the preferred approach as it can provide largely background-free PA-signals. Still, a common approach among the reported cavity-enhanced PA experiments has been to produce the PA-signal via intensity modulation of the laser. This can be achieved by on/off coupling of the laser beam to the cavity. In practice, the laser wavelength is swept over the cavity resonance modes at

half the modulation frequency, while quickly locking the laser to the cavity mode at resonance [70, 81–86]. The amplitude modulation approach is often reasonable since most PA detectors require fast wavelength modulation, which can be impossible to implement with the laser continuously locked to the resonance of a high finess cavity. The first reason is that the resonance frequency of the cavity would need to be tuned at the same speed, which in practice requires changing the cavity length. A fast movement of macroscopic objects, such as the cavity mirrors, can be difficult to achieve. The second reason is the extended time a photon resides inside the cavity. The scan speed, expressed in $\mathrm{cm^{-1}s^{-1}}$, must be much less than the ratio $\Delta\nu_c/\tau_{RD}$, where $\tau_{RD} = 1/(2\pi\Delta\nu_c)$ is the photon lifetime in the cavity, also known as the ring-down time. As an example, for a cavity with finesse $F = 1000$ and a length of 20 cm, $\Delta\nu_c/\tau_{RD} = 240$ kHz/670 ns = 12 $\mathrm{cm^{-1}s^{-1}}$. The 12 $\mathrm{cm^{-1}s^{-1}}$ limit is exceeded if the required modulation is at kHz frequencies and modulation amplitude in the order of $1 \times 10^{-2}\,\mathrm{cm^{-1}}$, as often is the case.

Unlike most other PAS methods, the CEPAS operates at low acoustic frequencies in the 10–100 Hz range, making it better suited for wavelength modulated cavity-enhanced PAS. In our experiments of Article **III**, the conditions for wavelength modulation were good since the constructed optical build-up cavity had a moderate BUF and we used CEPAS as a PA detector. The scanning speed at the implemented 30 Hz modulation frequency and 0.04 $\mathrm{cm^{-1}}$ modulation amplitude was about 1.2 $\mathrm{cm^{-1}s^{-1}}$, whereas the $\Delta\nu_c/\tau_{RD}$ limit for the cavity was 550 $\mathrm{cm^{-1}s^{-1}}$ ($\Delta\nu_c = 6$ MHz = 0.0002 $\mathrm{cm^{-1}}$). The wavelength modulation for the PA-signal generation was implemented by moving the back mirror of the cavity with a piezo electric actuator. Changing the cavity length changes its resonance frequency. Consequently, since the laser was continuously locked to the cavity, it followed the modulation and produced the desired wavelength modulation.

In the spectroscopic experiments of Article **III**, we used trace gas detection of acetylene (C_2H_2) and hydrogen cyanide (HCN) to demonstrate the performance enhancement by the use of build-up cavity method in CEPAS. We refer to this new method as cavity-enhanced CEPAS (CE-CEPAS). Our objective was to demonstrate two main aspects: the detection performance would increase proportional to the BUF and, simultaneously, the method could operate background-free in the wavelength modulation mode. In the measurements, we focused mainly on C_2H_2 as it is a highly inert gas and thus does not pose any additional challenges on gas handling and sampling.

In CE-CEPAS, recording of spectra has two practical approaches: a continuous high-resolution wavelength scan, and a mode-hop scan from one cavity mode to another. The first approach has a limited continuous tuning range as often the cavity resonance frequency cannot be shifted as much as the laser frequency. This is because of the short travel of the piezo actuators used in tuning the cavity length. In addition, a large scale movement of a cavity mirror would affect the BUF as the cavity becomes misaligned. The second approach has a low resolution determined by the cavity FSR. In our case, the FSR was 0.034 $\mathrm{cm^{-1}}$ which is in the order of the linewidth of a typical pressure broadened absorption line. On the other hand, sampling at each equally spaced cavity mode can provide an accurate relative frequency scale. An example of a 2nd harmonic spectrum recorded at the FSR resolution is given in Figure 4.8. The sample contained a small amount of C_2H_2 and HCN among some water residue. The

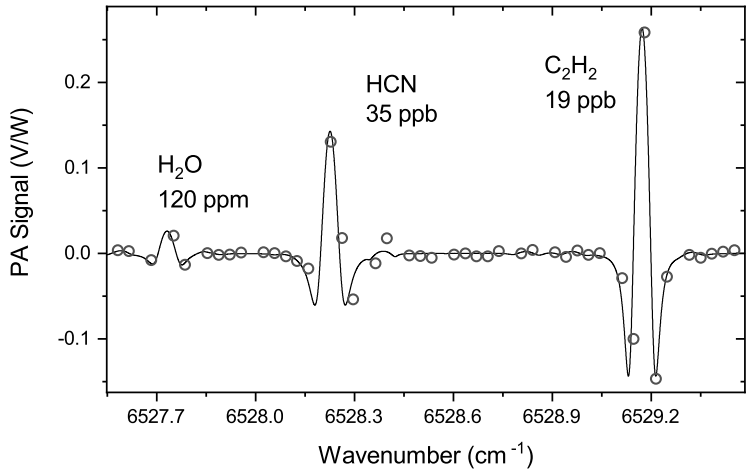

Figure 4.8: Measured (circles) and simulated (solid line) second harmonic CE-CEPAS spectrum sampled at cavity resonances.

spectrum was used to identify the targeted spectral lines. The result shows that the FSR limited resolution was sufficient for spectral identification, and that the wavelength modulation method also provides a background-free signal when implemented together with a build-up cavity. The continuous line illustrates the high resolution second harmonic signal, which was simulated based on a Voigt line profile and the HITRAN database [28].

The improvement in the detection sensitivity by the build-up cavity was verified by first calibrating the signal response with and without the build-up cavity. Then, an Allan deviation analysis was performed on a steady PA-signal at a low trace-gas concentration [78]. The measurements were carried out for C_2H_2 by recording the signal at the centre of the line. A BUF of about 100 was found from the calibration results, shown in Figure 4.9 a), by dividing the slope of the CE-CEPAS calibration by the slope of the CEPAS calibration. In the shown calibration curves, the CEPAS curve has been multiplied with the BUF for illustration purposes. The measured BUF matches well with the calculated value that was based on the mirror reflectivities and the cavity losses. The good agreement of the measured CE-CEPAS data to the linear fit shows that there was no reduction of the BUF in the measured concentration range.

The results of the Allan deviation analysis are shown in Figure 4.9 b). After dividing the CEPAS results with the BUF the curves for CEPAS and CE-CEPAS overlap, which shows that the use of the build-up cavity and wavelength modulation does not increase the noise in short time scale. Thus, performance of the CE-CEPAS system is improved directly by a factor equal to the BUF. The achieved noise equivalent mixing ratio for C_2H_2 was 240 ppt in 1 s measurement time. The respective NNEA value referenced to the 7.5 mW input power was $1.75 \times 10^{-12}\,\mathrm{Wcm^{-1}Hz^{-1/2}}$, which is better than any value reported for PAS before [70]. The difference between CEPAS and CE-CEPAS on a longer time scale of about 100 s indicates that the build-up cavity adds some long term instability to the system. This could result from the cavity resonance drifting off the transition line centre, since the cavity was not yet

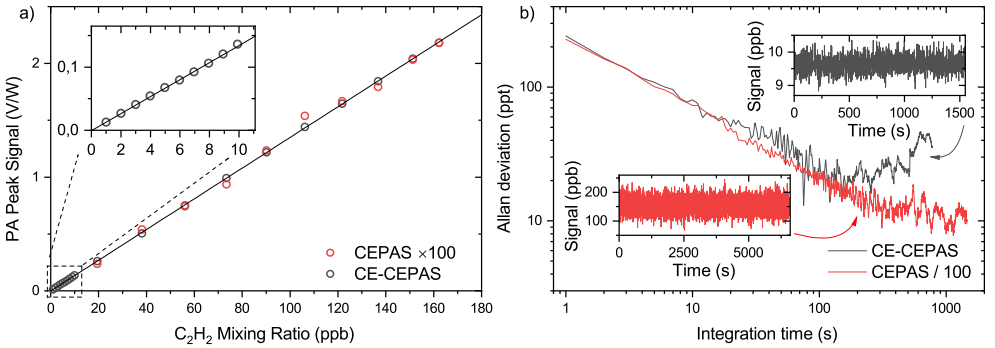

Figure 4.9: Results of the experiments with the optical build-up cavity for signal enhancement in CEPAS. a) Calibration curves with (CE-CEPAS) and without (CEPAS) the build-up cavity. The slope of the CEPAS curve has been multiplied with the BUF for comparison. b) Allan deviation analysis of a long CEPAS and CE-CEPAS measurement at a low C_2H_2 volume mixing ratio.

actively stabilised in the experiments reported here.

4.2 Hyphenation of gas chromatography and photo-acoustic spectroscopy

Laser spectroscopic trace gas analysers are mostly specialised in detection of one to three small molecules, such as CH_4 or CO_2. They are valued for their high detection sensitivity and selectivity. The performance is in most cases based on high resolution spectroscopy of narrow and isolated transitions of the targeted molecules. Larger molecules do not possess such fine structure, which is why laser spectroscopy-based trace gas analysers with narrow wavelength tuning range have not been a particularly popular tool for their analysis. The task becomes especially complicated if the sample contains several larger molecular weight compounds and especially if they have similar spectra. In such case, it is likely that the spectroscopic identification and quantification is limited to recognising just some molecular classes based on the characteristic spectral bands of their functional groups. An example is given in Figure 4.10, where we have simulated the absorbance spectrum of a complex gas mixture of light and heavy molecules. The simulation was based on data from the HITRAN and Pacific Northwest National Laboratory (PNNL) spectral databases. The blue line shows the total absorbance spectrum, that is the sum of the absorbance of the individual compounds shown in different colours. The spectra of the larger molecules are offset for clarity. The wavelength range was selected to match that of a broadly tunable external cavity (EC) QCL (EC-QCL), which currently represents the spectrally broadest mid-infrared laser technology that is suitable for portable trace gas analysers.

The heavier molecules included in the simulation, except cyclohexane, are all alcohols. Their broad absorption bands are quite similar as they originate from the same C-O stretching motion associated with the -OH group. This makes the interpretation of the combined spectrum difficult. In contrast, the sharp and isolated spectral lines

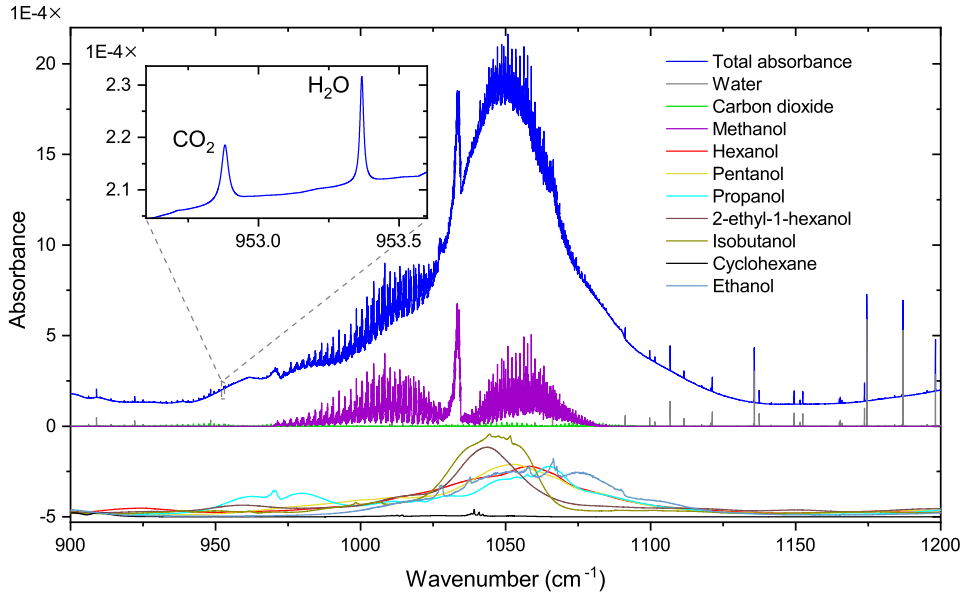

Figure 4.10: Simulated absorbance spectra of a mixture of light and heavy compounds. The spectra of the heavier molecules are offset for clarity.

of CO_2 and H_2O, shown in the inset, could be used for highly selective detection of CO_2 and H_2O with a basic narrowly tunable QCL. The background absorption level would not affect the measurements if a whole spectral line is recorded and fitted, or a wavelength modulation technique is used to null the background.

In general, the analysis of the aforementioned sample would be trivial with the standard tools in analytical chemistry. One such tool for universal analysis of chemical compounds is gas chromatography [94]. It is a physical separation method in which a gaseous sample is passed through a long thin tube, called a column. The function of the column is to retain the analytes of the sample by different amounts. As a result, they will emerge (elute) from the end of the column at different times as they are moved forward by a continuously flowing carrier gas. The method is applicable to molecular weights up to 1000 g/mol and can separate hundreds of components from a sample. The eluted components can be detected by various sensitive detectors. The separation process itself provides quantitative analysis and some identification capabilities for simple sample matrices if referenced to a calibration standard. For such applications, a simple non-selective detector, such as a flame ionisation detector (FID) or a thermal conductivity detector (TCD), is sufficient. In many cases, however, the sample matrix is more complex, and it is necessary to employ selective detectors. These include, for example, the popular mass spectrometer with superb absolute identification capability. The combination of GC and MS (GC-MS) currently provides the most versatile platform for quantitative analysis of chemical compounds and has therefore become the tool for many standardised methods.

Figure 4.11 shows a basic configuration of a gas chromatograph together with a typical chromatogram. The essential parts are carrier gas flow control, injector, oven,

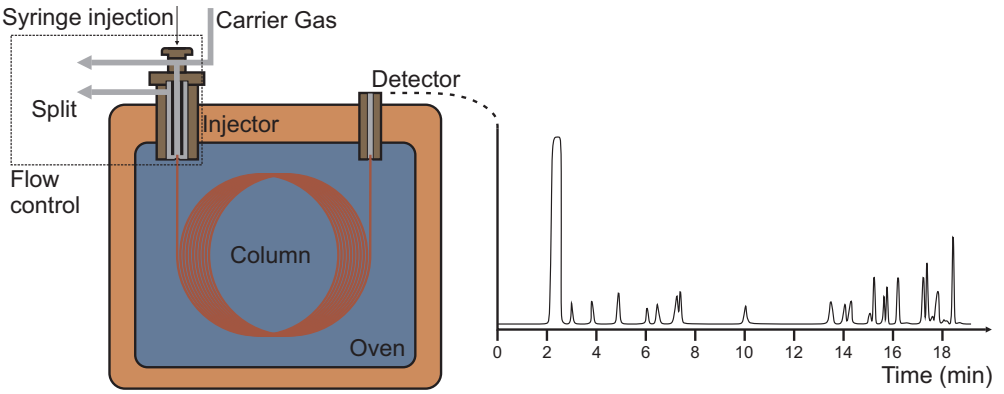

Figure 4.11: Schematic of a typical gas chromatograph and an example of a chromatogram.

column and detector. In short, a gas chromatograph functions as follows. An inert carrier gas, such as nitrogen or helium, is fed continuously to the GC where a flow control system carefully splits it in three ways: a small portion (∼1 ml/min) flows through the column and carries the injected sample, a portion (∼3 ml/min) flushes the septum of the heated injector of any residual sample, and a portion (∼100 ml/min) carries away excess sample from the inlet liner in split injection mode. The split injection is an injection technique that is often required with liquid samples to reduce the amount and time of the sample vaporised in the injector to enter the column. A long injection period would result in broad chromatographic peaks and poor separation. The column is typically a fused silica capillary column that is 15 to 30 m long and about 0.3 mm in inner diameter. On its inner surface there is a thin (0.2 µm) layer of high boiling point substance, called the stationary phase. The chromatographic separation is based on interactions of the analyte with the stationary phase, which depends on their relative vapour pressures and affinities for the stationary phase. The retention of the components is temperature dependent, which is why the column is placed in an oven that can have a varying programmable temperature profile from ambient to 360 °C. At the end of the column, a detector produces a signal proportional to the amount of analyte present in the effluents. The area of a chromatographic peak is proportional to the amount of the analyte, and the retention time provides information for identification of the analyte.

Our interest in gas chromatography is to extend the capabilities of laser based trace gas detectors to larger molecules while still maintaining the distinct benefits of LAS compared to many other analytical techniques: they require no consumables, they are compact and portable. From another perspective, our work leads towards the development of new selective infrared detectors for GC that are orders of magnitude more sensitive than the present FTIR based detectors.

Important classifications to understand in relation to GC detectors are whether the detector is concentration or mass flow sensitive, selective or universal, and destructive or nondestructive. Scientist working on LAS based trace gas analysis are accustomed to relating a detector performance to detectable concentration of the analyte. However,

many detectors are in fact sensitive to the absolute amount, or mass, of the analyte. As an example, consider a popular ionisation based GC detector the FID. In FID, the signal is generated by burning of the analytes in an oxy-hydrogen flame. The burning generates some ions in the process, which in turn generate an electric signal on a collector electrode. The detector is mass flow sensitive, as the analyte is destroyed in the detection process and the signal is generated by the absolute amount of the analyte entering the detector. The FID is generally regarded to be a universal detector as it responds to all organic compounds that burn in the oxy-hydrogen flame. Some common compounds giving no response include CO_x, NO_x and H_2O.

A mass spectrometer is another mass flow sensitive and destructive GC detector, whereas an FTIR is concentration sensitive and nondestructive. Although both offer high selectivity and molecular identification capabilities, only mass spectrometers have become an essential detector technology for GC. FTIRs are used merely in special applications where mass spectrometer fail to identify isobaric compounds, such as some substitutional isomers [95]. A major reason for the popularity of GC-MS must be the fact that MS has orders of magnitude better detection limits over FTIR. In addition, the spectral libraries for MS are currently much more comprehensive as majority of the FTIR spectral libraries are for solid or liquid form of the compounds, which makes the data unsuitable for the analysis in GC.

Typical detection limits are in the 0.1 pg [95], 10 pg [94], and 10 ng ranges [95] for the MS, FID, and FTIR, respectively. The poor sensitivity of the FTIR detectors is rooted in the immensely small gas volumes the GC operates on [39]. The volume of a GC detector needs to small enough so that two successively eluted compounds are not present in the detector at the same time. In other words, the detector should not impair the separation power of the GC. A practical compromise is often achieved by requiring that the cell volume equals at most the volume corresponding to a full width at half-height of the chromatographic peaks. For typical operating conditions of a GC, the volume is about 100 µl. Currently, such absorption cells are implemented with so called lightpipes that are about 10 cm long and 1 mm in internal diameter with a reflective gold coating on the inner surface to guide the light through the pipe.

For a good detection sensitivity, an infrared detector would require an absorption path length in the order of several meters, preferably in the hundreds or thousands of meters. It is impossible to achieve such optical paths lengths in the given volume with incoherent light sources of FTIRs. If the volume is exceeded, a make-up gas can fill up the extra volume. The chromatographic resolution is then preserved with the cost of lower detection sensitivity proportional to the dilution ratio of the sample. Hence, the FTIR detection performance is unavoidably poor.

Some remedy for the detection sensitivity has been offered by the recent development in vacuum ultraviolet (VUV) absorption spectroscopy [96]. In the VUV the absorption cross sections of the electronic transitions of molecules are much larger, leading directly to improved detection sensitivity in similar lightpipes as with FTIR detectors. The spectral characterisation and identification capabilities in the VUV region are, however, worse than in the infrared region.

Laser light is characterised by a high coherence and brightness. For this reason, laser absorption spectroscopy does not suffer from optical path length restrictions the same way as FTIR. With lasers, it is possible to attain path lengths up to kilometres with cavity enhanced techniques [80], possibly even in a sub-ml volume. On the other

hand, some laser spectroscopic techniques, such as photo-acoustic spectroscopy, do not require a long absorption path length for high detection sensitivity. For example, the NEA of $1.4 \times 10^{-10}\,\mathrm{cm}^{-1}$ that was demonstrated in Article **I** with a 10 cm long CEPAS cell would require an absorption length of ∼71 km with direct transmission spectroscopy (assuming an NEA of 1×10^{-3}).

Despite the advantages LAS can potentially provide, its application in GC detection has so far gained little attention. One of the main reasons has been the narrow spectral coverage of the most common lasers, resulting in incapability to spectrally identify numerous compounds. A typical tuning range of a common narrow band laser is a few cm^{-1} whereas an FTIR has a typical optical detection band from 6500–600 cm^{-1}. However, in recent years, the emergence of new broadband laser sources, such as mid-infrared frequency combs [97] and external cavity quantum cascade lasers [98], could change this.

The early work in the 1980s on laser absorption spectroscopy based GC detectors included various technical approaches. Some employed the optothermal effect in different configurations, such as optical heterodyne detection [99], direct temperature measurement of the heated sample gas [100], and intracavity intensity modulation in a HeNe laser [101]. Others employed the photo-acoustic effect [102, 103], or intracavity absorption spectroscopy in a He-Ne laser [104]. The results obtained with packed columns were good in the sense that the detection limits were comparable to those of common universal detectors, such as FID and TCD. However, the added benefit over these simple detectors was modest since the researchers were basically limited to gas lasers, such as He-Ne and CO_2 lasers, which offered little selectivity and identification capabilities. In addition, the detection performance would have been worse for modern capillary columns with smaller gas volumes.

In a more recent work by Wu et al. [105], the researchers connected a hollow optical waveguide directly to the end of a capillary to create a µl-size absorption cell with a length in the order of meters. In their work, the spectroscopy was performed with a QCL, and later, in the work by Mengali et al. [106], with a widely tunable EC-QCL. In another work by Zare et al. [107], a standard near-infrared cavity ring down spectrometer was coupled to a GC via a combustor. The goal was to analyse $^{13}C/^{12}C$ isotope ratios of organic compounds. Due to the large volume of the spectrometer the instrument was not, however, capable of analysing trace levels.

The potential of photo-acoustic spectroscopy as a GC detector was already recognised by one of the pioneers of photo-acoustic trace gas detection Lloyd B. Kreuzer [102]. Advantages of PAS include small detection volume and extremely high detection sensitivity as was demonstrated in, for example, Article **I** and in reference [9]. The combination is advanced by the fact that PAS does not depend on the absorption path length the same way as transmission spectroscopy [55]. Currently, the volume of the smallest PAS instruments is in the ten to few ml range [79, 108, 109] with some realisations in the sub-ml range [110, 111], and with potential for even smaller µl-size [65, 112]. Nevertheless, a combination of extremely high detection sensitivity and µl detection volume is yet to be realised.

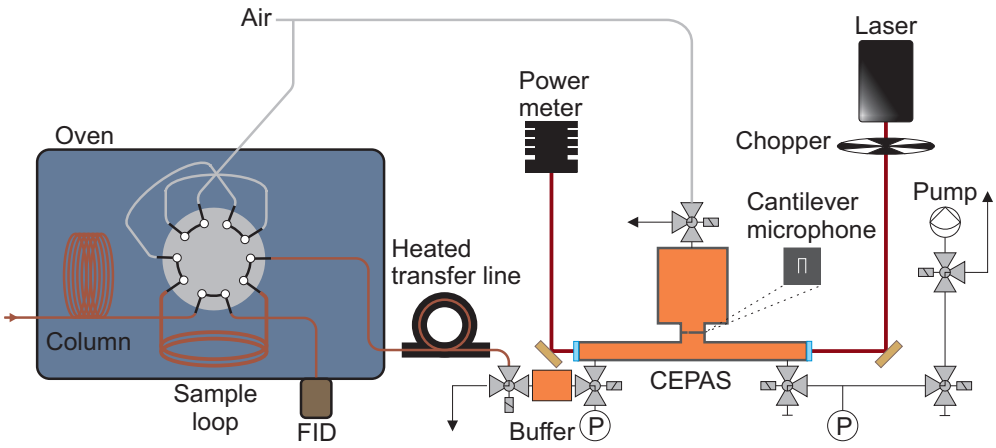

Figure 4.12: Experimental configuration of the GC-PAS system.

Detection of column effluents with cantilever-enhanced photo-acoustic spectroscopy

In the work of Article **IV**, which is summarised here, we took a step closer in developing a LAS based trace gas detector that is both highly sensitive and suitable for coupling with a GC. Our approach, for a proof-of-principle demonstration, was to use the same CEPAS cell as in Articles **I** and **III**. The gas exchange system was modified such that it can extract samples from a GC. We call the resulting hyphenation GC-PAS. We used a widely tunable EC-QCL (HedgeHog by Daylight Solutions) with a wavenumber range of 900–1200 cm^{-1} and a maximum CW output power of 130 mW. The laser provided a good combination of optical power and wavelength coverage, enabling strong photo-acoustic signal and comprehensive molecular identification capabilities. Unfortunately, the laser experienced frequent mode hops at intervals less than 1 cm^{-1}, which prevented its use for high-resolution spectroscopy. High-resolution spectroscopy could be useful for resolving the lightest molecules which commonly co-elute in a GC, as explained in connection to Figure 4.10.

The experimental configuration of our GC-PAS instrumentation is shown schematically in Figure 4.12. The effluents of a standard laboratory scale GC were sampled to the CEPAS detector by a 2-position 10-port rotary valve and a sample loop. The use of a sample loop was a necessary step in extracting the column effluents because the CEPAS detector cannot operate in a continuous gas flow. The loop had a volume of 0.44 ml, which means that at maximum a 30 s long portion of the effluents could be extracted at once. The portion not extracted flowed to a standard FID for monitoring and reference purposes. At the CEPAS detector, the extracted sample was first collected to an evacuated buffer cell of 1.28 ml in volume and filled with a make-up gas to 1800 mbar pressure. The make-up gas could be chosen to be either air or N_2 that was also the carrier gas of the GC. Air was used for most of the measurements. The buffer cell mixed the analyte with the make-up gas before feeding it to the CEPAS measurement cell. In the next step, the sample in the buffer cell was released to the evacuated CEPAS cell of 11 ml in total volume for the PA measurement. The end

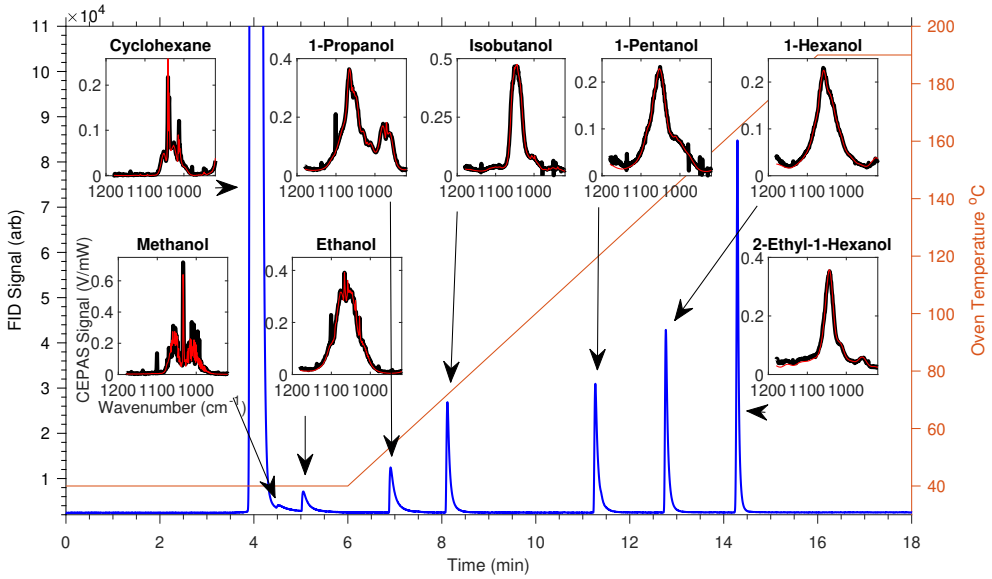

Figure 4.13: An example chromatogram for the alcohol mixture in cyclohexane (left axis) and the corresponding oven program (right axis). The insets show the measured optical power normalized CEPAS detector signals (spectra) for each peak. The black traces are measurements and the red traces fits from the PNNL database. The cyclohexane spectrum is from a different sample than the alcohols. Figure from Article **IV**.

pressure at equilibrium was about 200 mbar. It is clear that the non-optimised CEPAS cell had a too large volume for GC detection. We estimate that a cell volume of about 0.2 ml would have been ideal for the current setup, based on the volume of the eluted peaks. Therefore, we lost at least a factor of 50 in sensitivity with the current cell volume.

Each measurement at the detector involved scanning the laser frequency over its entire tuning range while recording the PA-signal at 85 Hz modulation frequency. A single scan took 75 s at $1\,\mathrm{cm}^{-1}$ resolution, while loading the gas took 35 s. The PA modulation was produced by cutting the laser intensity on/off with an optical chopper wheel at the 85 Hz rate. The use of the chopper was in this case necessary because wavelength modulation would have been ineffective for detection of large molecules with broad spectral features. In principle the modulation amplitude could be extended to match the width of the absorption bands. However, the laser did not quite have the sufficient tuning range for that, nor did it have a linear enough power spectrum to avoid severe residual amplitude modulation. After each measurement, the cell was flushed clean with the make-up gas before the next measurement. Flushing was the slowest step in the detection cycle, taking several minutes depending on the boiling point of the analyte. The process was hindered by the low 50 °C maximum temperature of the detector. In practise, one CEPAS measurement was performed for each GC run.

The performance of the proof-of-principle GC-PAS instrument was evaluated by

analysing a mixture of several alcohols in cyclohexane at about 0.26 % (mol/mol) concentration each. Figure 4.13 shows an example chromatogram of the solution measured with the FID. On the right axis is the temperature of the GC oven. The insets show a CEPAS measurement (black trace) for each of the peaks on the chromatogram. The spectra have been normalised with the measured optical power of the laser, and the background signal resulting from the laser intensity modulation has been subtracted. The red traces show a classical least squares (CLS) fit from the PNNL database. Each spectrum was recorded on a different GC run. The cyclohexane spectrum was recorded for a different sample solution, where its concentration was about 13 % (mol/mol). The samples were injected manually with a microlitre syringe using split injection with a 1:10 split ratio. The injection volume was 0.5 µl.

The results presented here demonstrate the separation power of GC and the identification and quantification power of the CEPAS detector. Compared to the example in Figure 4.10 with the same sample matrix, the GC-PAS instrument is well capable of quantifying all the compounds in the sample, whereas without separation the task would hardly be possible. The given alcohol example is still a simple case. In real life, there would often be tens or hundreds of different compounds and then, the co-elution of peaks becomes more and more likely. In such case, it is possible to apply chemometric multivariate analysis tools, such as CLS, principal component regression, or partial least squares, to resolve a small number of co-eluted peaks.

In Figure 4.14, we demonstrate the capabilities of infrared spectroscopy and multivariate CLS analysis in two cases of co-eluted analytes. Figure 4.14 a) demonstrates the case of common septum or column bleed [94], which was emulated by turning the septum flush off. The bleed components are typically cyclic siloxanes. In our case, D_3 (hexamethylcyclotrisiloxane) and D_5 (decamethylcyclopentasiloxane) were identified using previously reported vapor phase spectra [113]. The 30 to 50 times stronger absorption bands of the siloxanes severely overlap with the bands of the alcohols which, in this example case, was 1-pentanol. However, since the gas matrix has been identified, CLS routine correctly solved the relative proportions of the compounds. In Figure 4.14 b) the peaks of two compounds 2-ethyl-1-hexanol and 6-methyl-5-hepten-2-one (sulcatone) completely overlap on the FID signal, whereas on the infrared detector, the spectra are clearly separated from each other.

The data in Figure 4.13, measured at high SNR, were used to calibrate the system for each compound. The response of the detector was found linear by performing measurements with diluted samples (see Article **IV** for details). As a last step on the CEPAS detector evaluation, we determined the limits of detection by performing repeated measurements with a blank sample and N_2 as a make-up gas. The LODs were defined for each compound as 3 times the standard deviation (3σ) of the results of the CLS analysis on the spectra, which had their background signal subtracted and signal normalised with the optical power of the laser. For further analysis, the same was performed with the laser turned off, which reveals the intrinsic detector noise limited performance. The FID LODs were estimated as the SNR of the peak heights relative to the baseline. The results, summarised in Table 4.1, show that the CEPAS detector performance is already orders of magnitude better than that of the FTIR lightpipe detectors, which most commonly have the LOD in the order of 10 ng [95]. If the cell volume were optimised and the intrinsic noise level was reached, the LODs would improve 2 to 3 orders of magnitude. The detection sensitivity would then surpass

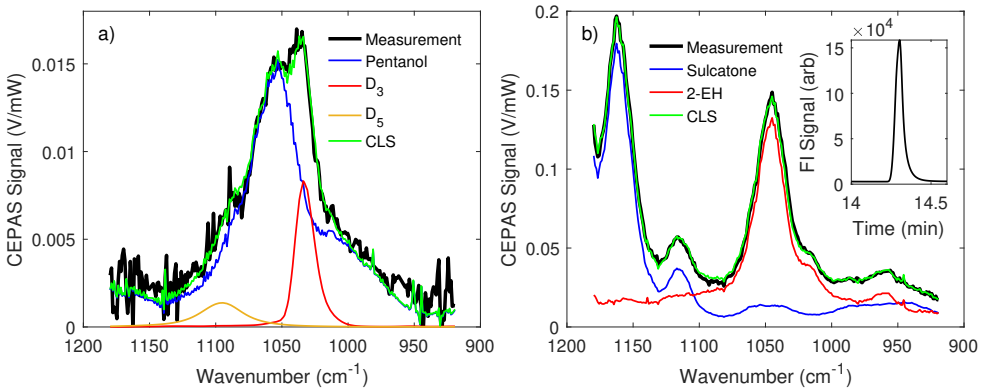

Figure 4.14: a) Measurement of 1-pentanol with interfering column/septum bleed. D_3: hexamethylcyclotrisiloxane, D_5: decamethylcyclopentasiloxane. b) Overlapping peaks on the FID (inset) well resolved with the CEPAS detector. 2-EH: 2-ethyl-1-hexanol. Figure from Article **IV**.

the FID. The differences between LODs of different compounds originate mainly from their absorption strengths and boiling points. Higher boiling point compounds seemed to experience more 'losses' most likely because of adsorption on the surfaces of the detector. It is also possible that the split injection partly discriminates the lower boiling point compounds from the higher ones. Article **IV** discusses the performance and LODs of the setup in more detail.

Table 4.1: Estimated limits of detection for the demonstrated GC-CEPAS. The units are expressed as on column masses. The CEPAS limited values express the intrinsic limit of the detector while the background N_2 values include experimental fluctuations from the gas exchange.

Compound	Background N_2 pg	CEPAS limited pg	FID estimates pg
Cyclohexane	7542	458	-
Methanol	181	12	145
Ethanol	292	16	44
Propanol	438	19	72
Isobutanol	325	18	23
Pentanol	956	46	24
Hexanol	1106	54	19
2-EH	2088	92	13

Chapter 5

Conclusions

Background-free spectroscopies have been demonstrated as a powerful tool for trace gas detection. Combined with high power lasers, they can be used to reach exceptional detection sensitivities beyond the capabilities of conventional direct absorption spectroscopy. Two background-free spectroscopic methods were investigated in different experimental scenarios for trace gas analysis: cantilever-enhanced photo-acoustic spectroscopy, and a novel broadband interferometric background suppression technique for absorption spectroscopy. Several sorts of MIR and NIR laser light sources were used in combination with these methods to access the ro-vibrational transitions of various molecules. From the perspective of trace gas detection, the most significant of the studied transitions are the strong fundamental transitions in the molecular fingerprint region around the atmospheric windows of 2000 to 3000 cm^{-1} and 800 to 1200 cm^{-1}. The developed highly sensitive trace gas detection methods can be applied in various fields, such as monitoring of indoor and outdoor air quality as well as industrial processes.

The novel broadband interferometric background suppression technique, presented in Article **II**, was discussed in Chapter 3. It can provide improved detection performance in direct absorption spectroscopy by optically subtracting the noisy background spectrum, which could otherwise saturate the photodetector and mask the absorption dips. The technique favours the use of high power laser light sources, such as optical frequency combs, and eases the dynamic range requirements for the detection system. The interferometric background suppression can be seen as an optical filtering technique, which does not restrict the choice of optical detection method. The method can be combined with various spectroscopic instruments, such as FTIRs, grating spectrometers, tunable laser absorption spectrometers, and dual-comb spectrometers. The suppression technique preserves the quantitative and calibration-free properties of direct absorption spectroscopy, which is exceptional in the category of background-free spectroscopies. The experimental results presented in Section 3.3 show about a factor of five improvement in the SNR compared to an absorption measurement without the suppression technique. The results are subject to further improvements by employing higher optical power and better interferometer optics, as discussed in Article **II**.

A majority of this thesis dealt with the application of cantilever-enhanced photo-acoustic spectroscopy to trace gas detection in various configurations. In Article

I, summarised in Section 4.1.1, the best reported noise-equivalent concentration in CEPAS [79] was pushed to a new level by using a high power CW-OPO in the detection of strongly absorbing HF. The exceptional sub-ppt level noise-equivalent concentration (NEC) achieved in our work demonstrated the great potential of CEPAS in high performance trace gas detection and motivates further research in the field. Similar or better results are expected for many other strongly absorbing molecules. The achieved NEC can be improved by solving some technical difficulties in, for example, the gas handling of the highly reactive HF, as discussed in Article **I**.

The work on CEPAS was continued in Article **III** with a more general approach for ultra low level trace gas detection. Instead of a direct use of a high power laser source, the optical power of a much more practical small near-infrared semiconductor laser was built up in an optical cavity to reach similar intra-cavity power levels and noise-equivalent absorbance (NEA) as in the previous CW-OPO work. This was the first time when a build-up cavity was used in conjunction with CEPAS, and the first time a wavelength modulation scheme was employed in cavity-enhanced photo-acoustic spectroscopy. In the results of Article **III**, summarised in Section 4.1.2, we reported so far the best normalised noise-equivalent absorption (NNEA) value for a photo-acoustic detector. The experiments were carried out in the NIR region for technical convenience, but a continuation of the work could include moving to the MIR region for stronger absorption lines.

In the work of Article **IV**, the attention was drawn to the detection of challenging compounds and gas matrices. The detection of large molecules is often challenging for LAS, especially in the case of a complex mixture. In our approach, we used a gas chromatograph to separate the compounds before detection with the CEPAS detector and a widely tunable EC-QCL. In the results, summarised in Section 4.2, we demonstrated a quantitative analysis of a complex mixture of alcohols at a detection sensitivity far better than what is possible with a conventional FTIR based infrared detector used in GC. The results compare favourably with the few other reported LAS based GC detectors. Still, major improvements are possible when the construction, and size of the CEPAS detector are optimised for the novel application, as well as some excess experimental noise is eliminated. Further research on the topic is highly motivated since LAS could allow the development a competitive GC detector for field applications as it is compact, offers good sensitivity, good selectivity, and requires no consumables.

Bibliography

[1] J. Hansen, M. Sato, P. Kharecha, G. Russell, D. W. Lea, and M. Siddall, "Climate change and trace gases," *Philosophical Transactions of the Royal Society A*, vol. 365, no. 1856, pp. 1925–1954, 2007.

[2] W. Ren, L. Luo, and F. K. Tittel, "Sensitive detection of formaldehyde using an interband cascade laser near 3.6 μm," *Sensors and Actuators B: Chemical*, vol. 221, pp. 1062–1068, 2015.

[3] C. B. Hirschmann, S. Sinisalo, J. Uotila, S. Ojala, and R. L. Keiski, "Trace gas detection of benzene, toluene, p-, m- and o-xylene with a compact measurement system using cantilever enhanced photoacoustic spectroscopy and optical parametric oscillator," *Vibrational Spectroscopy*, vol. 68, pp. 170–176, 2013.

[4] M. T. Smith, "Advances in understanding benzene health effects and susceptibility," *Annual Review of Public Health*, vol. 31, no. 1, pp. 133–148, 2010.

[5] B. Henderson, A. Khodabakhsh, M. Metsälä, I. Ventrillard, F. M. Schmidt, D. Romanini, G. A. D. Ritchie, S. te Lintel Hekkert, R. Briot, T. Risby, N. Marczin, F. J. M. Harren, and S. M. Cristescu, "Laser spectroscopy for breath analysis: towards clinical implementation," *Applied Physics B*, vol. 124, no. 8, p. 161, 2018.

[6] G. Berden, R. Peeters, and G. Meijer, "Cavity ring-down spectroscopy: Experimental schemes and applications," *International Reviews in Physical Chemistry*, vol. 19, no. 4, pp. 565–607, 2000.

[7] K. H. Michaelian, *Photoacoustic IR spectroscopy: instrumentation, applications and data analysis*. John Wiley & Sons, 2010.

[8] I. Galli, S. Bartalini, R. Ballerini, M. Barucci, P. Cancio, M. De Pas, G. Giusfredi, D. Mazzotti, N. Akikusa, and P. De Natale, "Spectroscopic detection of radiocarbon dioxide at parts-per-quadrillion sensitivity," *Optica*, vol. 3, no. 4, p. 385, 2016.

[9] L. Xiong, W. Bai, F. Chen, X. Zhao, F. Yu, and G. J. Diebold, "Photoacoustic trace detection of gases at the parts-per-quadrillion level with a moving optical grating," *Proceedings of the National Academy of Sciences of the United States of America*, vol. 114, no. 28, pp. 7246–7249, 2017.

[10] G. Litfin, C. R. Pollock, R. F. C. Jr., and F. K. Tittel, "Sensitivity enhancement of laser absorption spectroscopy by magnetic rotation effect," *The Journal of Chemical Physics*, vol. 72, no. 12, pp. 6602–6605, 1980.

[11] R. Lewicki, J. H. Doty, R. F. Curl, F. K. Tittel, and G. Wysocki, "Ultrasensitive detection of nitric oxide at 5.33 μm by using external cavity quantum cascade laser-based faraday rotation spectroscopy," *Proceedings of the National Academy of Sciences of the United States of America*, vol. 106, no. 31, pp. 12 587–12 592, 2009.

[12] Y. Wang, M. Nikodem, E. Zhang, F. Cikach, J. Barnes, S. Comhair, R. A. Dweik, C. Kao, and G. Wysocki, "Shot-noise limited faraday rotation spectroscopy for detection of nitric oxide isotopes in breath, urine and blood," *Scientific Reports*, vol. 5, no. 1, p. 9096, 2015.

[13] W. M. Fairbank, T. W. Hänsen, and A. L. Schawlow, "Absolute measurement of very low sodium-vapor densities using laser resonance fluorescence," *Journal of the Optical Society of America*, vol. 65, no. 2, pp. 199–204, 1975.

[14] W. Neuhauser, M. Hohenstatt, P. E. Toschek, and H. Dehmelt, "Localized visible Ba^+ mono-ion oscillator," *Physical Review A*, vol. 22, no. 3, pp. 1137–1140, 1980.

[15] P. Patimisco, G. Scamarcio, F. K. Tittel, and V. Spagnolo, "Quartz-enhanced photoacoustic spectroscopy: A review," *Sensors*, vol. 14, no. 4, pp. 6165–6206, 2014.

[16] V. Koskinen, J. Fonsen, K. Roth, and J. Kauppinen, "Progress in cantilever enhanced photoacoustic spectroscopy," *Vibrational Spectroscopy*, vol. 48, no. 1, pp. 16–21, 2008.

[17] I. Vurgaftman, R. Weih, M. Kamp, J. R. Meyer, C. L. Canedy, C. S. Kim, M. Kim, W. W. Bewley, C. D. Merritt, J. Abell, and S. Höfling, "Interband cascade lasers," *Journal of Physics D: Applied Physics*, vol. 48, no. 12, p. 123001, 2015.

[18] M. S. Vitiello, G. Scalari, B. Williams, and P. De Natale, "Quantum cascade lasers: 20 years of challenges," *Optics Express*, vol. 23, no. 4, pp. 5167–5182, 2015.

[19] R. F. Curl, F. Capasso, C. Gmachl, A. A. Kosterev, B. McManus, R. Lewicki, M. Pusharsky, G. Wysocki, and F. K. Tittel, "Quantum cascade lasers in chemical physics," *Chemical Physics Letters*, vol. 487, no. 1, pp. 1–18, 2010.

[20] B. Saleh and M. Teich, *Fundamentals of Photonics*, 2nd ed. John Wiley & Sons. Inc, 2007.

[21] M. Vainio and L. Halonen, "Mid-infrared optical parametric oscillators and frequency combs for molecular spectroscopy," *Physical Chemistry Chemical Physics*, vol. 18, no. 6, pp. 4266–94, 2016.

[22] T. Fortier and E. Baumann, "20 years of developments in optical frequency comb technology and applications," *Communications Physics*, vol. 2, no. 1, p. 153, 2019.

[23] N. Picqué and T. W. Hänsch, "Frequency comb spectroscopy," *Nature Photonics*, vol. 13, no. 3, pp. 146–157, 2019.

[24] T. Udem, R. Holzwarth, and T. W. Hänsch, "Optical frequency metrology," *Nature*, vol. 416, no. 6877, pp. 233–237, 2002.

[25] T. L. Nicholson, S. L. Campbell, R. B. Hutson, G. E. Marti, B. J. Bloom, R. L. McNally, W. Zhang, M. D. Barrett, M. S. Safronova, G. F. Strouse, W. L. Tew, and J. Ye, "Systematic evaluation of an atomic clock at 2×10^{-18} total uncertainty," *Nature Communications*, vol. 6, no. 1, p. 6896, 2015.

[26] J. M. Hollas, *Modern spectroscopy*, 4th ed. John Wiley & Sons, 2004.

[27] L. S. Rothman, C. Rinsland, A. Goldman, S. Massie, D. Edwards, J. Flaud, A. Perrin, C. Camy-Peyret, V. Dana, J.-Y. Mandin *et al.*, "The HITRAN molecular spectroscopic database and hawks (HITRAN atmospheric workstation): 1996 edition," *Journal of Quantitative Spectroscopy and Radiative Transfer*, vol. 60, no. 5, pp. 665–710, 1998.

[28] I. E. Gordon, L. S. Rothman, C. Hill, R. V. Kochanov, Y. Tan, P. F. Bernath, M. Birk, V. Boudon, A. Campargue, K. V. Chance, B. J. Drouin, J. M. Flaud, R. R. Gamache, J. T. Hodges, D. Jacquemart, V. I. Perevalov, A. Perrin, K. P. Shine, M. A. H. Smith, J. Tennyson, G. C. Toon, H. Tran, V. G. Tyuterev, A. Barbe, A. G. Császár, V. M. Devi, T. Furtenbacher, J. J. Harrison, J. M. Hartmann, A. Jolly, T. J. Johnson, T. Karman, I. Kleiner, A. A. Kyuberis, J. Loos, O. M. Lyulin, S. T. Massie, S. N. Mikhailenko, N. Moazzen-Ahmadi, H. S. P. Müller, O. V. Naumenko, A. V. Nikitin, O. L. Polyansky, M. Rey, M. Rotger, S. W. Sharpe, K. Sung, E. Starikova, S. A. Tashkun, J. V. Auwera, G. Wagner, J. Wilzewski, P. Wcisło, S. Yu, and E. J. Zak, "The HITRAN2016 molecular spectroscopic database," *Journal of Quantitative Spectroscopy and Radiative Transfer*, vol. 203, pp. 3–69, 2017.

[29] J. Tennyson, P. F. Bernath, A. Campargue, A. G. Császár, L. Daumont, R. R. Gamache, J. T. Hodges, D. Lisak, O. V. Naumenko, L. S. Rothman *et al.*, "Recommended isolated-line profile for representing high-resolution spectroscopic transitions (iupac technical report)," *Pure and Applied Chemistry*, vol. 86, no. 12, pp. 1931–1943, 2014.

[30] M. Bolshov, Y. A. Kuritsyn, and Y. V. Romanovskii, "Tunable diode laser spectroscopy as a technique for combustion diagnostics," *Spectrochimica Acta Part B: Atomic Spectroscopy*, vol. 106, pp. 45–66, 2015.

[31] P. Kluczynski, J. Gustafsson, Å. M. Lindberg, and O. Axner, "Wavelength modulation absorption spectrometry—an extensive scrutiny of the generation of signals," *Spectrochimica Acta Part B: Atomic Spectroscopy*, vol. 56, no. 8, pp. 1277–1354, 2001.

[32] E. De Tommasi, A. Castrillo, G. Casa, and L. Gianfrani, "An efficient approximation for a wavelength-modulated 2nd harmonic lineshape from a voigt absorption profile," *Journal of Quantitative Spectroscopy and Radiative Transfer*, vol. 109, no. 1, pp. 168–175, 2008.

[33] J. Westberg, J. Wang, and O. Axner, "Fast and non-approximate methodology for calculation of wavelength-modulated voigt lineshape functions suitable for real-time curve fitting," *Journal of Quantitative Spectroscopy and Radiative Transfer*, vol. 113, no. 16, pp. 2049–2057, 2012.

[34] G. B. Rieker, J. B. Jeffries, and R. K. Hanson, "Calibration-free wavelength-modulation spectroscopy for measurements of gas temperature and concentration in harsh environments," *Applied Optics*, vol. 48, no. 29, pp. 5546–5560, 2009.

[35] T. T. Fricke, N. D. Smith-Lefebvre, R. Abbott, R. Adhikari, K. L. Dooley, M. Evans, P. Fritschel, V. V. Frolov, K. Kawabe, J. S. Kissel, B. J. J. Slagmolen, and S. J. Waldman, "DC readout experiment in enhanced LIGO," *Classical and Quantum Gravity*, vol. 29, no. 6, p. 065005, 2012.

[36] R. W. Boyd, "Intuitive explanation of the phase anomaly of focused light beams," *Journal of the Optical Society of America*, vol. 70, no. 7, pp. 877–880, 1980.

[37] E. Serabyn and M. M. Colavita, "Fully symmetric nulling beam combiners," *Applied Optics*, vol. 40, no. 10, pp. 1668–1671, 2001.

[38] D. Mawet, C. Hanot, C. Lenaerts, P. Riaud, D. Defrère, D. Vandormael, J. Loicq, K. Fleury, J.-Y. Plesseria, J. Surdej, and S. Habraken, "Fresnel rhombs as achromatic phase shifters for infrared nulling interferometry," *Optics Express*, vol. 15, no. 20, pp. 12 850–12 865, 2007.

[39] P. R. Griffiths and J. A. De Haseth, *Fourier transform infrared spectrometry*, 2nd ed. John Wiley & Sons Ltd, 2007.

[40] H. R. Chandrasekhar, L. Genzel, and J. Kuhl, "Double-beam fourier spectroscopy with interferometric background compensation," *Optics Communications*, vol. 17, no. 1, pp. 106–110, 1976.

[41] D. Kuehl and P. R. Griffiths, "Dual-beam fourier transform infrared spectrometer," *Analytical Chemistry*, vol. 50, no. 3, pp. 418–422, 1978.

[42] L. Genzel and J. Kuhl, "A new version of a michelson interferometer for fourier transform infrared spectroscopy," *Infrared Physics*, vol. 18, no. 2, pp. 113–120, 1978.

[43] Z. Guan, M. Lewander, and S. Svanberg, "Quasi zero-background tunable diode laser absorption spectroscopy employing a balanced michelson interferometer," *Optics Express*, vol. 16, no. 26, pp. 21 714–21 720, 2008.

[44] J. Hayden, S. Hugger, F. Fuchs, and B. Lendl, "A quantum cascade laser-based Mach–Zehnder interferometer for chemical sensing employing molecular absorption and dispersion," *Applied Physics B*, vol. 124, no. 2, p. 29, 2018.

[45] M. Zhu, A. Kleczewski, and R. C. Taber, "System for performing optical spectroscopy including interferometer," U.S. Patent US 9,341,516 B2, 2016.

[46] T. Buberl, P. Sulzer, A. Leitenstorfer, F. Krausz, and I. Pupeza, "Broadband interferometric subtraction of optical fields," *Optics Express*, vol. 27, no. 3, pp. 2432–2443, 2019.

[47] I. Coddington, N. Newbury, and W. Swann, "Dual-comb spectroscopy," *Optica*, vol. 3, no. 4, pp. 414–426, 2016.

[48] A. V. Muraviev, V. O. Smolski, Z. E. Loparo, and K. L. Vodopyanov, "Massively parallel sensing of trace molecules and their isotopologues with broadband subharmonic mid-infrared frequency combs," *Nature Photonics*, vol. 12, no. 4, pp. 209–214, 2018.

[49] Q. Ru, Z. E. Loparo, X. Zhang, S. Crystal, S. Vasu, P. G. Schunemann, and K. L. Vodopyanov, "Self-referenced octave-wide subharmonic gap optical parametric oscillator centered at 3 μm and pumped by an Er-fiber laser," *Optics Letters*, vol. 42, no. 22, pp. 4756–4759, 2017.

[50] F. C. Cruz, D. L. Maser, T. Johnson, G. Ycas, A. Klose, F. R. Giorgetta, I. Coddington, and S. A. Diddams, "Mid-infrared optical frequency combs based on difference frequency generation for molecular spectroscopy," *Optics Express*, vol. 23, no. 20, pp. 26 814–26 824, 2015.

[51] V. Smolski, S. Vasilyev, I. Moskalev, M. Mirov, Q. Ru, A. Muraviev, P. Schunemann, S. Mirov, V. Gapontsev, and K. Vodopyanov, "Half-watt average power femtosecond source spanning 3–8 μm based on subharmonic generation in gaas," *Applied Physics B*, vol. 124, no. 6, p. 101, 2018.

[52] M. Seidel, X. Xiao, S. A. Hussain, G. Arisholm, A. Hartung, K. T. Zawilski, P. G. Schunemann, F. Habel, M. Trubetskov, V. Pervak, O. Pronin, and F. Krausz, "Multi-watt, multi-octave, mid-infrared femtosecond source," *Science Advances*, vol. 4, no. 4, p. eaaq1526, 2018.

[53] A. G. Bell, "Upon the production and reproduction of sound by light," *Journal of the Society of Telegraph Engineers*, vol. 9, no. 34, pp. 404–426, 1880.

[54] F. J. Harren, G. Cotti, J. Oomens, and S. Lintel Hekkert, *Photoacoustic Spectroscopy in Trace Gas Monitoring.* John Wiley & Sons Ltd, 2006, pp. 2203–2226.

[55] D. C. Dumitras, D. C. Dutu, C. Matei, A. M. Magureanu, M. Petrus, and C. Popa, "Laser photoacoustis spectroscopy: principles, instrumentation, and characterization," *Journal of Optoelectronics and Advanced Materials*, vol. 9, no. 12, pp. 3655–3701, 2007.

[56] S. Schilt, J. P. Besson, and L. Thévenaz, "Near-infrared laser photoacoustic detection of methane: the impact of molecular relaxation," *Applied Physics B*, vol. 82, no. 2, pp. 319–328, 2005.

[57] G. Wysocki, A. A. Kosterev, and F. K. Tittel, "Influence of molecular relaxation dynamics on quartz-enhanced photoacoustic detection of CO_2 at λ=2 μm," *Applied Physics B*, vol. 85, no. 2, pp. 301–306, 2006.

[58] A. Miklós, P. Hess, and Z. Bozóki, "Application of acoustic resonators in photoacoustic trace gas analysis and metrology," *Review of Scientific Instruments*, vol. 72, no. 4, pp. 1937–1955, 2001.

[59] A. Miklós, "Acoustic aspects of photoacoustic signal generation and detection in gases," *International Journal of Thermophysics*, vol. 36, no. 9, pp. 2285–2317, 2015.

[60] B. D. Adamson, J. E. Sader, and E. J. Bieske, "Photoacoustic detection of gases using microcantilevers," *Journal of Applied Physics*, vol. 106, no. 11, 2009.

[61] P. Sievilä, N. Chekurov, J. Raittila, and I. Tittonen, "Sensitivity-improved silicon cantilever microphone for acousto-optical detection," *Sensors and Actuators A: Physical*, vol. 190, pp. 90–95, 2013.

[62] A. A. Kosterev, Y. A. Bakhirkin, R. F. Curl, and F. K. Tittel, "Quartz-enhanced photoacoustic spectroscopy," *Optics Letters*, vol. 27, no. 21, pp. 1902–1904, 2002.

[63] K. Wilcken and J. Kauppinen, "Optimization of a microphone for photoacoustic spectroscopy," *Applied Spectroscopy*, vol. 57, no. 9, pp. 1087–1092, 2003.

[64] K. Chen, Z. Yu, Z. Gong, and Q. Yu, "Lock-in white-light-interferometry-based all-optical photoacoustic spectrometer," *Optics Letters*, vol. 43, no. 20, pp. 5038–5041, 2018.

[65] S. Zhou, M. Slaman, and D. Iannuzzi, "Demonstration of a highly sensitive photoacoustic spectrometer based on a miniaturized all-optical detecting sensor," *Optics Express*, vol. 25, no. 15, pp. 17 541–17 548, 2017.

[66] R. A. Coutu, I. R. Medvedev, and D. T. Petkie, "Improved sensitivity mems cantilever sensor for terahertz photoacoustic spectroscopy," *Sensors (Basel)*, vol. 16, no. 2, p. 251, 2016.

[67] W. Li, Z. Wang, C. Feng, Q. Li, and H. Yu, "High sensitivity all-optical acoustic pressure sensor based on resonant micro-opto-mechanical cantilever with integrated rib waveguide," *Sensors and Actuators A: Physical*, vol. 285, pp. 300–307, 2019.

[68] V. Koskinen, J. Fonsen, K. Roth, and J. Kauppinen, "Cantilever enhanced photoacoustic detection of carbon dioxide using a tunable diode laser source," *Applied Physics B: Lasers & Optics*, vol. 86, no. 3, pp. 451–454, 2007.

[69] J. Kauppinen, K. Wilcken, I. Kauppinen, and V. Koskinen, "High sensitivity in gas analysis with photoacoustic detection," *Microchemical Journal*, vol. 76, no. 1–2, pp. 151–159, 2004.

[70] Z. Wang, Q. Wang, W. Zhang, H. Wei, Y. Li, and W. Ren, "Ultrasensitive photoacoustic detection in a high-finesse cavity with pound-drever-hall locking," *Optics Letters*, vol. 44, no. 8, pp. 1924–1927, 2019.

[71] R. W. Boyd and D. Prato, *Nonlinear Optics*. San Diego, United States: Elsevier Science & Technology, 2008.

[72] L. E. Myers, R. C. Eckardt, M. M. Fejer, R. L. Byer, W. R. Bosenberg, and J. W. Pierce, "Quasi-phase-matched optical parametric oscillators in bulk periodically poled LiNbO3," *Journal of the Optical Society of America B*, vol. 12, no. 11, pp. 2102–2116, 1995.

[73] O. Gayer, Z. Sacks, E. Galun, and A. Arie, "Temperature and wavelength dependent refractive index equations for MgO-doped congruent and stoichiometric LiNbO3," *Applied Physics B*, vol. 91, no. 2, pp. 343–348, 2008.

[74] W. Chen, J. Cousin, E. Poullet, J. Burie, D. Boucher, X. Gao, M. W. Sigrist, and F. K. Tittel, "Continuous-wave mid-infrared laser sources based on difference frequency generation," *Comptes Rendus Physique*, vol. 8, no. 10, pp. 1129 – 1150, 2007, optical parametric sources for the infrared.

[75] W. R. Bosenberg, A. Drobshoff, J. I. Alexander, L. E. Myers, and R. L. Byer, "93% pump depletion, 3.5-W continuous-wave, singly resonant optical parametric oscillator," *Optics Letters*, vol. 21, no. 17, pp. 1336–1338, 1996.

[76] A. K. Y. Ngai, S. T. Persijn, G. von Basum, and F. J. M. Harren, "Automatically tunable continuous-wave optical parametric oscillator for high-resolution spectroscopy and sensitive trace-gas detection," *Applied Physics B*, vol. 85, no. 2-3, pp. 173–180, 2006.

[77] I. Breunig, D. Haertle, and K. Buse, "Continuous-wave optical parametric oscillators: recent developments and prospects," *Applied Physics B*, vol. 105, no. 1, p. 99, 2011.

[78] P. Werle, R. Mücke, and F. Slemr, "The limits of signal averaging in atmospheric trace-gas monitoring by tunable diode-laser absorption spectroscopy (TDLAS)," *Applied Physics B*, vol. 57, no. 2, pp. 131–139, 1993.

[79] J. Peltola, T. Hieta, and M. Vainio, "Parts-per-trillion-level detection of nitrogen dioxide by cantilever-enhanced photo-acoustic spectroscopy," *Optics letters*, vol. 40, no. 13, pp. 2933–2936, 2015.

[80] G. Gagliardi and H.-P. Loock, Eds., *Cavity-enhanced spectroscopy and sensing*, ser. Springer Series in Optical Sciences. Springer, 2014, vol. 179.

[81] A. Rossi, R. Buffa, M. Scotoni, D. Bassi, S. Iannotta, and A. Boschetti, "Optical enhancement of diode laser-photoacoustic trace gas detection by means of external fabry-perot cavity," *Applied Physics Letters*, vol. 87, no. 4, p. 041110, 2005.

[82] M. Hippler, C. Mohr, K. A. Keen, and E. D. McNaghten, "Cavity-enhanced resonant photoacoustic spectroscopy with optical feedback CW diode lasers: A novel technique for ultratrace gas analysis and high-resolution spectroscopy," *The Journal of Chemical Physics*, vol. 133, no. 4, p. 044308, 2010.

[83] A. Kachanov, S. Koulikov, and F. K. Tittel, "Cavity-enhanced optical feedback-assisted photo-acoustic spectroscopy with a 10.4 μm external cavity quantum cascade laser," *Applied Physics B*, vol. 110, no. 1, pp. 47–56, 2013.

[84] S. Borri, P. Patimisco, I. Galli, D. Mazzotti, G. Giusfredi, N. Akikusa, M. Yamanishi, G. Scamarcio, P. De Natale, and V. Spagnolo, "Intracavity quartz-enhanced photoacoustic sensor," *Applied Physics Letters*, vol. 104, no. 9, 2014.

[85] P. Patimisco, S. Borri, I. Galli, D. Mazzotti, G. Giusfredi, N. Akikusa, M. Yamanishi, G. Scamarcio, P. De Natale, and V. Spagnolo, "High finesse optical cavity coupled with a quartz-enhanced photoacoustic spectroscopic sensor," *Analyst*, vol. 140, no. 3, pp. 736–43, 2015.

[86] J. Hayden, B. Baumgartner, J. P. Waclawek, and B. Lendl, "Mid-infrared sensing of CO at saturated absorption conditions using intracavity quartz-enhanced photoacoustic spectroscopy," *Applied Physics B*, vol. 125, no. 9, p. 159, 2019.

[87] R. W. Fox, C. W. Oates, and L. W. Hollberg, "Stabilizing diode laser to high-finesse cavities," in *Cavity-Enhanced Spectroscopies*, ser. Experimental Methods in the Physical Sciences. Academic press, 2002, vol. 40, pp. 1–46.

[88] H. Kogelnik and T. Li, "Laser beams and resonators," *Applied Optics*, vol. 5, no. 10, pp. 1550–1567, 1966.

[89] J. Arnaud, W. Hubbard, G. Mandeville, B. De la Claviere, E. Franke, and J. Franke, "Technique for fast measurement of gaussian laser beam parameters," *Applied Optics*, vol. 10, no. 12, pp. 2775–2776, 1971.

[90] J. M. Khosrofian and B. A. Garetz, "Measurement of a gaussian laser beam diameter through the direct inversion of knife-edge data," *Applied Optics*, vol. 22, no. 21, pp. 3406–3410, 1983.

[91] I. Pupeza, "Power scaling of enhancement cavities for nonlinear optics," Ph.D. dissertation, Ludwig-Maximilians-Universität München, 2011.

[92] R. W. P. Drever, J. L. Hall, F. V. Kowalski, J. Hough, G. M. Ford, A. J. Munley, and H. Ward, "Laser phase and frequency stabilization using an optical resonator," *Applied Physics B*, vol. 31, no. 2, pp. 97–105, 1983.

[93] G. Giusfredi, I. Galli, D. Mazzotti, P. Cancio, and P. De Natale, "Theory of saturated-absorption cavity ring-down: radiocarbon dioxide detection, a case study," *Journal of the Optical Society of America B*, vol. 32, no. 10, pp. 2223–2237, 2015.

[94] H. M. McNair and J. M. Miller, *Basic gas chromatography*, 2nd ed. John Wiley & Sons, 2009.

[95] J. S. Zavahir, Y. Nolvachai, and P. J. Marriott, "Molecular spectroscopy – information rich detection for gas chromatography," *TrAC Trends in Analytical Chemistry*, vol. 99, pp. 47 – 65, 2018.

[96] K. A. Schug, I. Sawicki, D. D. Carlton Jr, H. Fan, H. M. McNair, J. P. Nimmo, P. Kroll, J. Smuts, P. Walsh, and D. Harrison, "Vacuum ultraviolet detector for gas chromatography," *Analytical Chemistry*, vol. 86, no. 16, pp. 8329–8335, 2014.

[97] A. Schliesser, N. Picqué, and T. W. Hänsch, "Mid-infrared frequency combs," *Nature Photonics*, vol. 6, no. 7, p. 440, 2012.

[98] A. Hugi, R. Maulini, and J. Faist, "External cavity quantum cascade laser," *Semiconductor Science and Technology*, vol. 25, no. 8, p. 083001, 2010.

[99] H. Lin, J. Gaffney, and A. Campillo, "Phase-fluctuation optical heterodyne spectrometer as a non-destructive detector for gas chromatography," *Journal of Chromatography A*, vol. 206, no. 2, pp. 205–214, 1981.

[100] V. Zharov and S. Montanari, "Capillar gas chromatography with laser optothermal detection," *Laser Chemistry*, vol. 5, no. 3, pp. 133–142, 1985.

[101] K. Fung and J. Gaffney, "Non-destructive gas chromatographic detection using laser intracavity photothermal spectroscopy," *Journal of Chromatography A*, vol. 363, no. 2, pp. 207–215, 1986.

[102] L. B. Kreuzer, "Laser optoacoustic spectroscopy for GC detection," *Analytical Chemistry*, vol. 50, no. 6, pp. 597A–606A, 1978.

[103] V. Zharov, S. Montanari, and V. Letokhov, "Application of IR laser optoacoustic spectroscopy in gas chromatography," *Laser Chemistry*, vol. 1, no. 3, pp. 163–176, 1983.

[104] J. D. Parli, D. W. Paul, and R. B. Green, "Helium-neon laser intracavity absorption detector for gas chromatography," *Analytical Chemistry*, vol. 54, no. 12, pp. 1969–1972, 1982.

[105] S. Wu, A. Deev, M. Haught, and Y. Tang, "Hollow waveguide quantum cascade laser spectrometer as an online microliter sensor for gas chromatography," *Journal of Chromatography A*, vol. 1188, no. 2, pp. 327–330, 2008.

[106] S. Mengali, N. Liberatore, D. Luciani, R. Viola, G. C. Cardinali, I. Elmi, A. Poggi, S. Zampolli, E. Biavardi, E. Dalcanale *et al.*, "Rapid screening and identification of illicit drugs by IR absorption spectroscopy and gas chromatography," in *Quantum Sensing and Nanophotonic Devices X*, vol. 8631. International Society for Optics and Photonics, 2013, p. 86312F.

[107] R. N. Zare, D. S. Kuramoto, C. Haase, S. M. Tan, E. R. Crosson, and N. M. Saad, "High-precision optical measurements of $^{13}C/^{12}C$ isotope ratios in organic compounds at natural abundance," *Proceedings of the National Academy of Sciences*, vol. 106, no. 27, pp. 10 928–10 932, 2009.

[108] X. Yang, Y. Xiao, Y. Ma, Y. He *et al.*, "A miniaturized QEPAS trace gas sensor with a 3D-printed acoustic detection module," *Sensors*, vol. 17, no. 8, p. 1750, 2017.

[109] J. Rouxel, J.-G. Coutard, S. Gidon, O. Lartigue, S. Nicoletti, B. Parvitte, R. Vallon, V. Zéninari, and A. Gliére, "Development of a miniaturized differential photoacoustic gas sensor," *Procedia Engineering*, vol. 120, pp. 396–399, 2015.

[110] A. Gorelik, A. Ulasevich, F. Nikonovich, M. Zakharich, V. Firago, N. Kazak, and V. Starovoitov, "Miniaturized resonant photoacoustic cell of inclined geometry for trace-gas detection," *Applied Physics B*, vol. 100, no. 2, pp. 283–289, 2010.

[111] A. Gorelik, A. Ulasevich, A. Kuz'muk, and V. Starovoitov, "A miniature prototype of a resonance photoacoustic cell for gas sensing," *Optics and Spectroscopy*, vol. 115, no. 4, pp. 567–573, 2013.

[112] G. Gruca, K. Heeck, J. Rector, and D. Iannuzzi, "Demonstration of a miniature all-optical photoacoustic spectrometer based on ferrule-top technology," *Optics Letters*, vol. 38, no. 10, pp. 1672–1674, 2013.

[113] F. Bernard, D. K. Papanastasiou, V. C. Papadimitriou, and J. B. Burkholder, "Infrared absorption spectra of linear (l2–l5) and cyclic (d3–d6) permethylsiloxanes," *Journal of Quantitative Spectroscopy and Radiative Transfer*, vol. 202, pp. 247–254, 2017.